8-2018

Feasibility Study of Laser-Fabricated Micro-Needles as an Electrospray Thruster

Andrew Joseph Broadbent
University of Tennessee, abroadb1@vols.utk.edu

To the Graduate Council:

I am submitting herewith a thesis written by Andrew Joseph Broadbent entitled "Feasibility Study of Laser-Fabricated Micro-Needles as an Electrospray Thruster." I have examined the final electronic copy of this thesis for form and content and recommend that it be accepted in partial fulfillment of the requirements for the degree of Master of Science, with a major in Aerospace Engineering.

Trevor M. Moeller, Major Professor

We have read this thesis and recommend its acceptance:

Lino Costa, L. Montgomery Smith

Accepted for the Council:
Dixie L. Thompson

Vice Provost and Dean of the Graduate School

(Original signatures are on file with official student records.)

Feasibility Study of Laser-Fabricated Micro-Needles as an Electrospray Thruster

A Thesis Presented for the

Master of Science

Degree

The University of Tennessee, Knoxville

Andrew Joseph Broadbent

August 2018

Acknowledgements

I would first like to thank Dr. Trevor M. Moeller for serving as my advisor, and providing a research assistantship opportunity, as well as giving guidance and advice to further my professional development. Thank you to my parents, Andrew P. and Robin A. Broadbent, and my sister, Ashlen N. Broadbent, for their constant support and encouragement that helped me throughout the many difficulties of research. Thank you, as well, to Dr. Lino Costa and Dr. Monty Smith for serving on my committee. I would also like to thank my “brother,” Matthew “Kase” Cosgrove, and my extended “family” of friends for their continued support throughout graduate school, and in life.

Abstract

Capable of carrying small-scale instruments, micro-satellites, often called CubeSats for their shape, provide an excellent platform for a variety of educational and research missions. However, once placed in orbit satellites experience small amounts of drag that slow the craft down, and deteriorate its orbit over time. The addition of a propulsion system will allow a CubeSat to correct and maintain orbit, as well as perform other maneuvers. Due to their size and power requirements, CubeSats cannot accommodate conventional propulsion methods. Instead, these satellites rely on electric propulsion to provide a compact, low power thruster for making orbital adjustments. Of particular interest to this research are electrospray thrusters. Because of their size, electrospray thrusters can easily be clustered together to form large arrays to make up for the small amounts of thrust, making them ideal for CubeSats.

Microfabrication techniques developed at UTSI allow preparation of arrays of emitters suitable for electrospray applications, and exhibiting critical dimensions that can potentially enable smaller, denser arrays requiring less space and power. In this work, these needles were modeled and simulated under an applied voltage to determine if they can be used as electric field enhancers in a thruster. Using procedures established from references, the optimal emitter spacing was also determined.

Table of Contents

List of Tables

List of Figures

Nomenclature

Symbol	Description	Units
A	Fowler-Nordheim Equation Constant	A/eV
A_v	Legendre Polynomial Constant	
a	Array Configuration Parameter	
B	Fowler-Nordheim Equation Constant	eV nm
B_v	Legendre Polynomial Constant	
b	Emitter Spacing	m
c	Array Configuration Parameter	
D	Diameter	m
d	Extractor Grid Spacing	m
E	Electric Field	V/m
F	Force	N
g	Geometric Factor	
h	Planck's Constant	J s
	Emitter Height	m
j	Current Density	A/m^2
K	Conductivity	S/m
k	Boltzmann Constant	J/K
M	Ion Mass	kg
N	Ion Density	m^{-3}
P/A	Power Required per Area	W/m^2
R_c	Radius of Curvature	m
R^*	Critical Radius	m
r	radius	m
T	Temperature	K
T/A	Thrust Density	N/m^2
V	Voltage	V
v	Velocity	m/s

Greek

Symbol	Description	Units
α	Cone Semi-Angle	Degree
β	Field Enhancement Factor	
γ	Surface Tension	Dyne/cm
ε	Relative Permittivity	
ε_0	Permittivity of Free Space	s^2/m^2
κ	Dielectric Constant	
ν	Legendre Polynomial Constant	
	Material Dependent Parameter	
ρ	Density	kg/m^3
σ_s	Surface Charge Density	C/m^2

Φ	Electric Potential	V
	Material Dependent Parameter	

Chapter 1: Introduction

The purpose of this research is to investigate the feasibility of using micro-needle-shaped emitters as electric field enhancers in an electrospray thruster. This is accomplished through modelling an array of needles and simulating the electric field strength at the needle tips. The minimum spacing at which maximum field enhancement occurs was also determined by varying the needle spacing in the simulations until a spacing was found at which field enhancement ceases to show any significant increase.

1.1: Overview

Over the past two decades, small-scale satellites such as CubeSats and other micro-satellites have become popular vehicles for performing a variety of missions. Advances in micro-electromechanical systems (MEMS) technology and fabrication, applied to development of electric propulsion methods has allowed for the miniaturization of equipment normally used on larger satellites [1]. This allows for the launch and deployment of multiple satellites for a given launch, resulting in cost savings due to the reduced payload mass, which in turn allows for reduced fuel mass for the launch vehicle.

CubeSats (Figure 1) in particular are quite popular due to their simple, yet modular, design. CubeSat units or “U”s are 10 x 10 x 10 cm^3 cubes with a mass of approximately 1 kg [2]. These satellites can be built to fit mission profiles including global positioning, formation flying, imaging, deep space exploration, and communications [3]. Their simplicity lends them to be excellent educational resources, allowing a student to participate in the entire mission cycle of the satellite [4].

Figure 1: Cal Poly CubeSat, CP1. [5]

Miniaturizing a satellite's components requires miniaturizing its propulsion systems, which has produced challenges in design due to size, weight, and power limitations. Microsatellites require low thrust, high specific impulse (I_{sp}), and high efficiency thrusters, lending electric propulsion to be the preferred method on satellites this size. Larger electric propulsion methods such as Hall Thrusters and Ion engines have too much mass and require too much power to use on satellites this small, and they don't scale down well. Pulsed Plasma Thrusters (PPT) are a simple and proven technology, but require high voltage and typically have lower efficiencies [3]. Field Effect Electric Propulsion (FEEP) thrusters provide high efficiency, but are limited in how well they can be clustered. Colloid and electrospray thrusters provide a compact, high I_{sp}, high efficiency thruster at the cost of low thrust- on the order of ~1 μN or less. This is often overcome by clustering multiple thrusters together in order to achieve higher thrusts when necessary [3].

1.2: Motivation

The Center for Laser Applications (CLA) at the University of Tennessee Space Institute (UTSI) utilizes a femtosecond laser setup for micromachining. Included in this setup are a 1.2 W, 250 kHz amplified femtosecond laser (Figure 2a), and a 20 W, 200 kHz – 2 MHz fiber laser (Figure 2b). The lasers are capable of 5 µJ, 160 fs pulses at a 790 nm wavelength, and 100 µJ, 325 fs - 10 ps pulses at a 1030 nm wavelength, respectively. These lasers have been used to machine precise surface Nano-pores to create a mold in which the needle-like polymer fibers are formed. See Figure 3. These Nano-fibers can be manufactured in length from 1 – 60 µm, with aspect ratios up, *h/D*, to 200, where *h* and *D* are the emitter height and diameter, respectively.

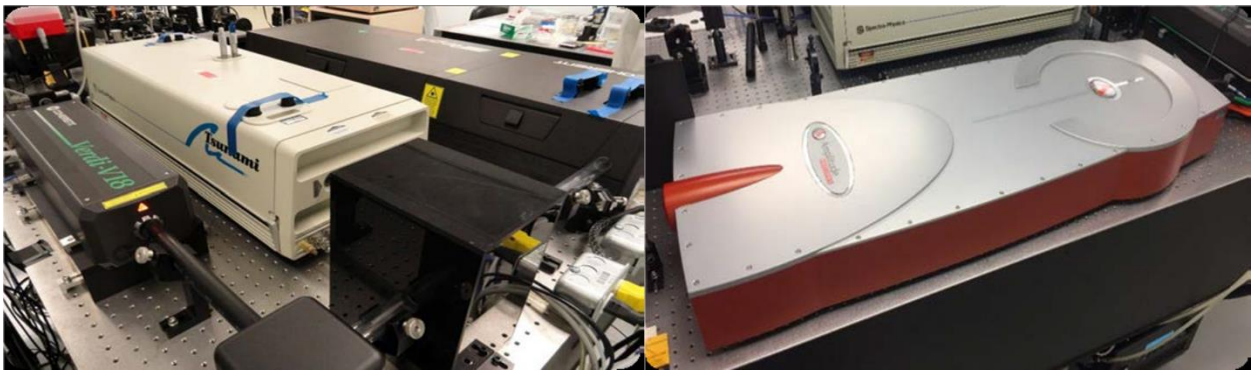

Figure 2: Lasers used in CLA's micromachining setup (a) Left: 1.2 W, 250 kHz amplified femtosecond laser. (b) Right: 20 W, 200 kHz - 2 MHz fiber laser.

Electrospray thrusters using micro-scale needles as electric field enhancers have been designed and tested [2, 6-8]. However, these thrusters typically operate with an applied voltage of 1 kV or higher, and they have needles that are typically tens to a couple hundred micrometers long, and 10 µm or greater in diameter. The research presented herein looks to determine if it is possible to use shorter needles to achieve

the same or higher electric field concentration using voltages in the range of 100 to 200 V. Smaller needles will result in smaller thruster packaging, and lower voltage requirements will allow for smaller power supplies and lower bus voltages. Thus, the reduction in size and weight of the thrusters and power supply will allow more capacity for instrumentation on a CubeSat.

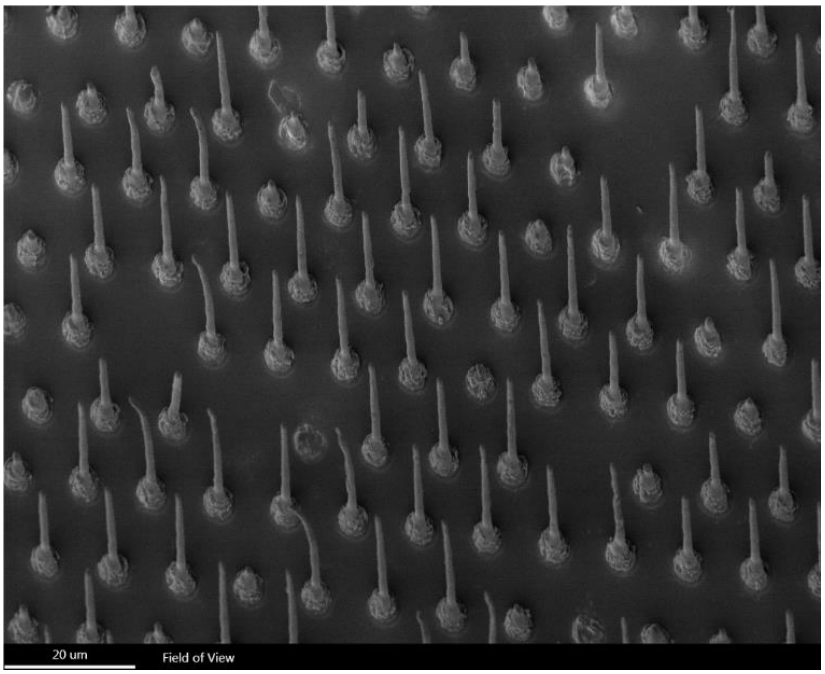

Figure 3: 25° tilt SEM image of 20 μm long nanofibers prepared at UTSI.

1.3: Scope

The purpose of this study was to perform a feasibility study on the use of micro-needles as electric field enhancers. Numerical simulations were run on single needles and arrays of needles to determine spacing effects, and the resulting electric fields are compared with the analytical model in Chapter 2 to determine if a given configuration will provide enough enhancement to perform as an electrospray thruster. Results were compared with existing data to determine any improvements in performance. Beyond

the scope of this thesis are the physical design, construction, and testing of the thruster concept.

1.4: Organization

This thesis is organized as follows. Chapter 2 provides background and theory on electrospray thrusters. The simulation models and setup are given in Chapter 3 with results discussed in Chapter 4. Finally, Chapter 5 presents conclusions and future work.

Chapter 2: Background

2.1: Electrostatic Acceleration

Electrostatic acceleration forms the basis for electrospray thrusters. A typical thruster will contain an ion source, accelerator grid, neutralizer, and a voltage source. Figure 4 provides a schematic of a one-dimensional electrostatic thruster geometry. Here, the ion source is located at position $x = 0$ where a positive voltage $V = V_0$ is applied. The accelerator electrode is positioned at a distance d from the ion source and is grounded so that $V = 0$. The resulting electric field, $E = -(dV/dx)$, pulls the ions away from the source, and accelerates them in the streamwise direction. At steady state conditions, the current density $j = Nqv$, remains constant over the distance x. Once past the accelerator grid, the neutralizer cathode emits electrons to neutralize ions and prevent charge build-up on the spacecraft. Thrust output from this method depends only on exhaust velocity, mass of the ion, and total ion flux the system can handle [9].

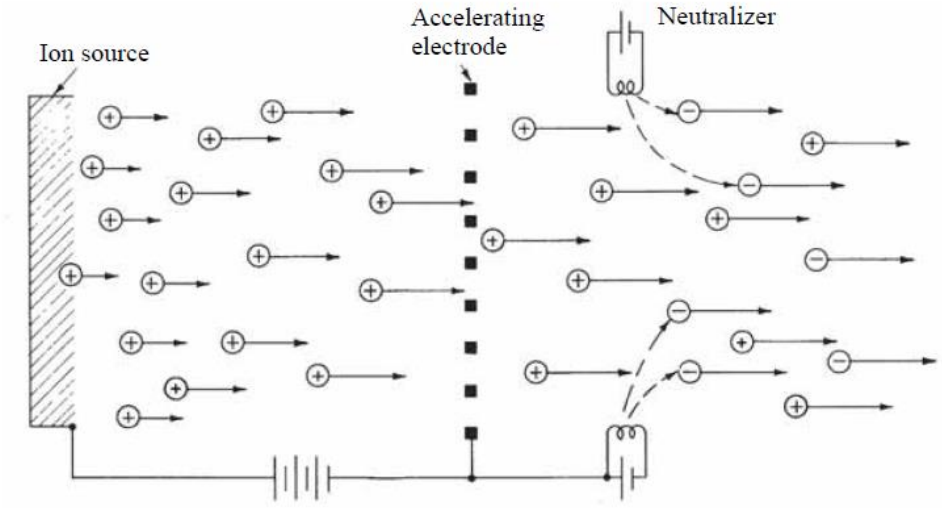

Figure 4: Electrostatic accelerator schematic. [9]

The velocity of an ion at any point can be found through integration of Newton's laws of motion. Given an ion of charge, *q* in Coulombs, and mass *M* in kg, the velocity, *v(x)* in m/s, is,

$$v(x) = \left[\frac{2q(V_0 - V)}{M}\right]^{\frac{1}{2}} \tag{1}$$

where *V* and V_0 are the potential at location *x* and source potential, respectively, in volts. This equation assumes negligible velocity at the source. Poisson's Equation relates potential and electric field,

$$\nabla \cdot E = -\nabla^2 V = \frac{\bar{q}}{\kappa \varepsilon_0} \tag{2}$$

where $\bar{q}$ is the charge density in C/m^3, ε_0 is the permittivity of free space with units s^2/m^2, and κ is the dielectric constant (dimensionless). In the case of zero charge density associated with a neutral plasma or vacuum, Laplace's equation results,

$$\nabla \cdot E = -\nabla^2 V = 0 \tag{3}$$

However, when the charge density is non-zero, such as in the acceleration region of an electrostatic thruster, Poisson's equation must be retained. Equation (2) can be written to relate the potential profile and ion density profile,

$$\frac{d^2V}{dx^2} = -\frac{Nq}{\varepsilon_0} = -\frac{j}{\varepsilon_0 v} = -\frac{j}{\varepsilon_0}\left[\frac{M}{2q(V_0 - V)}\right]^{\frac{1}{2}} \tag{4}$$

where *N* is the ion density, *j* is the current density, and *v* is the velocity of the ion given by equation (1). Multiplying equation (4) by the integration factor *2(dV/dx)* and integrating provides the relation,

$$\left(\frac{dV}{dx}\right)^2 - \left(\frac{dV}{dx}\right)_0^2 = \frac{4j}{\varepsilon_0}\left[\frac{M(V_0 - V)}{2q}\right]^{\frac{1}{2}} \tag{5}$$

where $E_0^2=(dV/dx)_0^2$, and E_0 is the electric field at the source. Assuming negligible ion velocity at the source, in order for current to exist, E_0 must fall in the range:

$$0 < E_0 < \frac{V_0}{d} \tag{6}$$

where d is the position of the accelerating electrode. The upper limit, V_0/d, provides the electrostatic field between a one-dimensional gap with zero space charge. The lower limit represents the *space-charge limited* case, where charges at the source plane neutralize the accelerating field, with the electric potential at the acceleration grid shielded by intervening ions. In this case:

$$\frac{dV}{dx} = 2\left(\frac{j}{\varepsilon_0}\right)^{\frac{1}{2}}\left[\frac{M(V_0 - V)}{2q}\right]^{\frac{1}{4}} \tag{7}$$

Integrating equation (7) through separation of variables results in:

$$V = V_0 - \left[\frac{3}{2}\left(\frac{j}{\varepsilon_0}\right)^{\frac{1}{2}}\left(\frac{M}{q}\right)^{\frac{1}{4}} x\right]^{\frac{4}{3}} \tag{8}$$

At $x = d$, $V = 0$. Substituting these values into equation (8) and solving for j results in the space-charge limited current density relation known as Child's Law [9]:

$$j = \frac{4\varepsilon_0}{9}\left(\frac{2q}{M}\right)^{\frac{1}{2}}\frac{V_0^{\frac{3}{2}}}{d^2} \tag{9}$$

This is the maximum current that can be drawn between two electrodes with potential difference V_0 and inter-electrode distance d. Therefore it is the state of maximum thrust for an electrostatic thruster. Figure 5 illustrates these relations. At negligible charge density, the electric field remains constant across the gap, while voltage decreases linearly. Under space-charge limited conditions, the electric field starts near zero, but increases rapidly and to a higher value than at negligible charge

density. Voltage no longer decreases linearly, velocity shows a shallower increase, while ion density decreases rapidly across x_a.

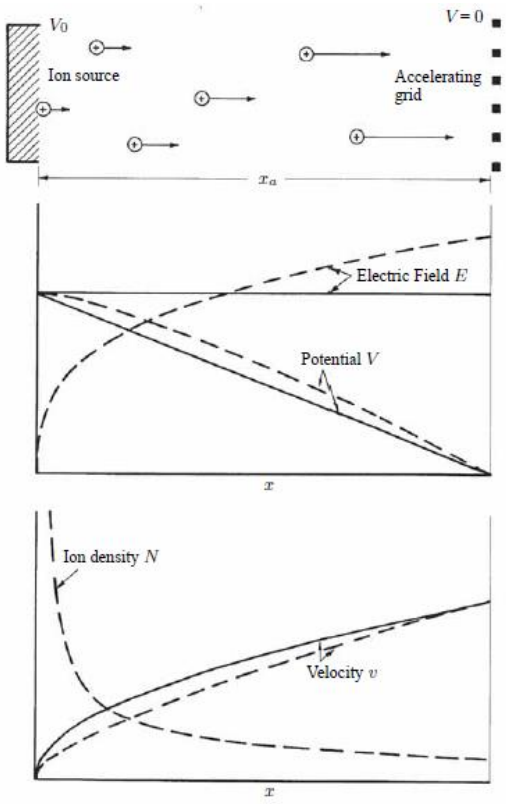

Figure 5: Potential, field, velocity, and ion density profiles for negligible charge density (---) and for space-charge limit (- - -) in one-dimensional ion acceleration. [9]

Ion current density restrictions from equation (9) imply a limit on thrust density. Using equations (1) and (9) along with definitions for thrust and current, the thrust density is,

$$\frac{T}{A} = \dot{m}v_a = \frac{jMv_a}{q} = \frac{8\varepsilon_0}{9}\left(\frac{V_0}{x_0}\right)^2 \tag{10}$$

where $\dot{m}$ is the mass flow rate per area, and is defined as N_aMv_a. Note that thrust density does not depend on charge-to-mass ratio when the electrode spacing is fixed. Charge-to-mass ratio does affect exhaust velocity, which is defined as,

$$v_a = \left(\frac{2qV_0}{M}\right)^{1/2} \tag{11}$$

Power required per area also depends on this ratio,

$$\frac{P}{A} = \frac{Tv_a}{2A} = \frac{4\varepsilon_0}{9}\left(\frac{2q}{M}\right)^{1/2}\frac{V_0^{3/2}}{x_a^2} \tag{12}$$

From equation (7), the maximum field occurs at the accelerating electrode and is defined as,

$$E_a = -\left(\frac{dV}{dx}\right)_a = \frac{4}{3}\frac{V_0}{x_a} \tag{13}$$

This limit also imposes a limit on thrust density

$$\frac{T}{A} = \frac{1}{2}\varepsilon_0 E_a^2 \tag{14}$$

2.2: Electrospray Thrusters

Electrospray thrusters use a two-step process to produce thrust: Ion generation and ion extraction. A voltage is applied to the propellant source to generate ions. The resulting electric field between the propellant source and accelerating grid extracts and accelerates the ions [2]. In order to extract ions, electric fields on the order of 1 V/nm are needed on the liquid's surface [10]. These strong fields are achieved by using sharp, pointed surfaces where electric fields concentrate near the tip. Three main structures for sharp tip field enhancement exist (Figure 6): internally fed capillary emitters, externally fed emitters, and porous emitters.

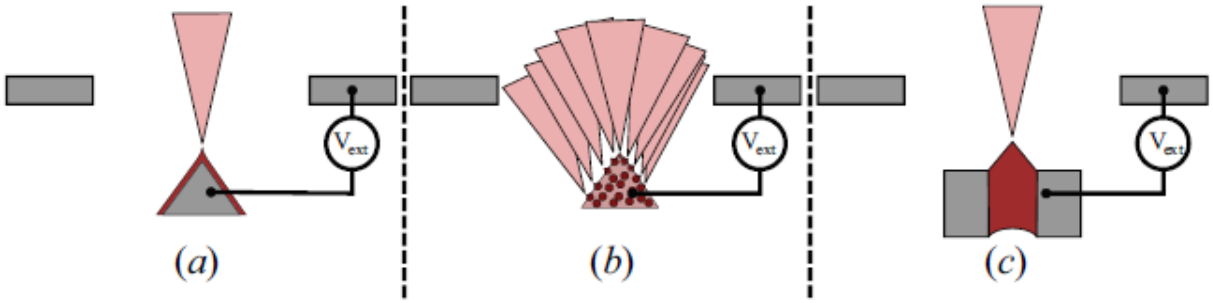

Figure 6: Common types of electrosprays. (a) Externally wetted, (b) Porous, and (c) Internally wetted. [11]

While each type of emitter has different mechanisms regarding how propellant is brought to the surface, once there ion emission process is the same. A voltage is applied between ion source and extractor, generating an electric field. The electric field pulls on the liquid, causing it to form a meniscus at the tip of the extractor. Once the electric field becomes strong enough to overcome the surface tension, a Taylor Cone is formed, and ions are extracted and accelerated downstream towards the extractor electrode. Extracted ions reach velocities in the km/s range, but only produce μN of thrust. Clustering electrospray thrusters together can help overcome the low levels of thrust [2].

2.2.1: Taylor Cones

Zeleny first described the phenomenon of Taylor Cones in 1914, who observed the discharge of liquid from a pointed metal tip when subjected to an electric potential [12]. When a voltage is applied between the pointed emitter and extractor, resulting electrostatic forces on the liquid balance surface tension forces, described by Equation (15), where R_{c1} and R_{c2} are the two principle radii. The initial pull of the electrostatic field causes the liquid at the tip to form a meniscus. Once electric field forces exceed

surface tension, the meniscus snaps into a cone shape and begins discharging ions. George Taylor, for whom the phenomenon is named, performed a series of experiments in 1964 [13] and determined that the cone formed has a semi-angle of 49.29°. Additionally, he determined that this angle is independent of liquid parameters or field [13].

$$\frac{\varepsilon_0 E_n^2}{2} = \gamma \left[\frac{1}{R_{c1}} + \frac{1}{R_{c2}}\right] \tag{15}$$

where E_n is the normal electric field, and γ is the surface tension of the liquid. $1/R_c$ is zero along the generator of a cone (line r in Figure 7, for example). The remaining radius describes the curvature of the normal section by Meusnier's theorem, resulting in $1/R_c = \cot(\alpha)/r$ [14]. Substituting this into Equation (15) and solving for the electric field normal to the surface results in [3]:

$$E_n = \sqrt{\frac{2\gamma \cot(\alpha)}{\varepsilon_0 r}} \tag{16}$$

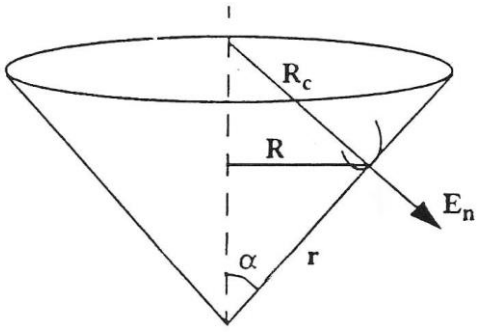

Figure 7: Normal electric field in a cone surface. [3]

Since the cone's surface is equipotential, solutions to the Laplacian in Equation (3) take on an axis-symmetric form of:

$$\Phi_v = A_v P_v(cos(\varphi))r^v + B_v Q_v(cos(\varphi))r^v \quad (17)$$

P_v and Q_v are first and second order Legendre polynomials, respectively, A_v and B_v are constants, and φ is the azimuthal angle. The first order polynomial P_v has its singularity outside of the cone, thus it can be removed from the equation. The perpendicular component of the electric field turns out to be the φ-component of the field, resulting in the derivation:

$$E_n = -\frac{1}{r}\frac{\partial \Phi}{\partial \varphi} = B_v \frac{dQ_v}{d\,cos(\varphi)} sin(\varphi)\, r^{v-1} \quad (18)$$

Using the relation between r and E_n from Equation (15), the only value of v that satisfies equation (18) is 0.5. Thus, the potential is equal to:

$$\Phi = Br^{\frac{1}{2}} Q_{\frac{1}{2}}(cos\,\varphi) \quad (19)$$

Provided electrode geometry is symmetric, Equation (19) provides a valid solution so long as analysis is also away from the jet region and there are no space charge effects [3]. A zero occurs at a value of φ = 49.29°, the same value determined experimentally by Taylor. As mentioned, Taylor determined that this value is independent of liquid properties; however, experimental evidence from De La Mora indicates that this is more of an ideal situation, and that the liquid's conductivity can affect the angle [15]. Experiments performed by Gamero et al. and De La Mora et al. have demonstrated that the angle depends on liquid flow rate, as space charge effects influence cone shape at higher flow rates [15],[16].

2.2.2: Surface Instability

When applied to a flat liquid surface, a strong enough electric field will cause free ions of the attracted polarity to concentrate on the surface. This concentration is called the surface charge density, and is denoted by σ_s. Equation (20) shows Gauss' Law:

$$\nabla \cdot \vec{E} = \frac{\rho}{\varepsilon_0} \tag{20}$$

which can be used to find surface charge density using the relation [17]:

$$\sigma_s = \varepsilon_0 E_0 \tag{21}$$

where E_0 is the electric field at the surface.

Any deformation of the liquid surface will result in a stronger electric field along the protruding parts. It is for this reason that electrospray thrusters use needle-like geometries as electric field enhancers. The traction of surface charge on a conductor is given by Equation (21), and intensifies along protruding areas. Once surface tension forces are unable to counter traction, the process becomes unstable. The extending section will grow into a shape dependent on the field and its surroundings [17]

$$\frac{1}{2}\sigma_s E = \frac{1}{2}\varepsilon_0 E^2 \tag{22}$$

Assuming a small, sinusoidal ripple on a curved surface, the electric field strength at which instabilities start due to perturbations exceeding surface tension is given by:

$$E_\infty > \sqrt{\frac{\pi\gamma}{\varepsilon_0 D}} \tag{23}$$

where D is the diameter of the surface ripple [17]. A complete derivation of Equation (23) is provided in Appendix A. In the context of electrospray thrusters, Equation (23) provides a minimum electric field strength required to generate a Taylor Cone.

2.2.3: Starting Voltage

To generate an electric field, a voltage must be applied across a gap. Thus, if a minimum electric field to induce an instability exists, there must also be a corresponding voltage. The needles used as field enhancers in electrospray thrusters can be modelled as a prolate spheroid. From Martinez-Sanchez [17], for a radius of curvature, R_c, and tip-to-extractor spacing, d, if $R_c << d$ then the electric field at the tip of an emitter can be described by:

$$E_{tip} = -\frac{2V/R_c}{ln(4d/R_c)} \tag{24}$$

Equation (24) is fully derived in Appendix A. This electric field must be strong enough to overcome surface tension in order for a Taylor Cone to form. Thus, assuming R_{c1} and R_{c2} in Equation (15) are equal due to symmetry, the following relation between tip electric field and surface tension can be established:

$$\frac{1}{2}\varepsilon_0 E_{tip}^2 > \frac{2\gamma}{R_c} \tag{25}$$

Substituting Equation (24) into equation (25) and solving for voltage, V, the required voltage to generate instabilities for a prolate spheroid of given radius of curvature, and extractor spacing is [17]:

$$V_{start} = \sqrt{\frac{\gamma R_c}{\varepsilon_0}}\, ln\left(\frac{4d}{R_c}\right) \tag{26}$$

2.3: Ionic Liquids

Early electrospray thrusters used liquid metals, such as Gallium [18], as liquid metal ion sources (LMIS). While capable of producing ions needed for electrospray propulsion, liquid metals require much higher onset voltages due to their higher surface

tension. Additionally, liquid metals often require heating in order to achieve a liquid state. This reduces overall efficiency since more power is needed to produce ions. Because of the need to heat liquid metals to their melting point, the selection of compatible sources is limited as few species of liquid metals having melting points low enough for use in an electrospray thruster [19].

Other liquid ion sources have been studied and include Tributyl Phosphate (TBP), glycerol, and Formamide [16]. Glycerol was among the early fuel sources studied, alongside LMISs, but was found to have poor conductivities resulting in onset voltages of 10 kV and higher. TBP has a low vapor pressure, helping to prevent losses from evaporation; however, its low dielectric constant prevents it from reaching necessary conductivities. More recently Formamide has been used as a fuel source, as it has higher conductivity and at low flow rates can achieve 50%-70% efficiency. When doped with sodium iodide (NaI), Formamide can reach conductivities up to 2.9 S/m. Formamide unfortunately suffers from losses through evaporation regardless of flow rate and conductivity. Additionally, as pointed out by Velasquez-Garcia, Formamide has proven cancerigenous effects, requiring careful handling of the substance [20].

A relatively new type of substance called Ionic Liquids has been utilized in electrospray thrusters to great effect. Over the past decade, these substances have been studied and characterized in electrospray thruster applications as ion sources, and are often referred to as Ionic Liquid Ionic Sources (ILIS). An ionic liquid is an organic salt with a melting point close to room temperature, and is composed of only charged species. No solvents are present in an ionic liquid. Additionally, the species of an ionic liquid are typically large, asymmetric and complex. As an example, the ionic liquid 1-

Ethyl-3-Methyl-Imidazolium Tetraflouroborate ($C_6H_{11}BF_4N_2$), referred to as EMI-BF_4, is shown in Figure 8. These characteristics provide several advantages when used in electrospray thrusters [21]:

1. Near zero vapor pressure: Ionic liquids exhibit almost zero vapor pressure, allowing them to be used in the vacuum of space without fear of evaporation losses.
2. Temperature range: As stated ILISs are liquids at room temperature, eliminating the need for any heating as with liquid metals. Some ILIS will remain liquid even at temperatures below -50° C. Additionally, ionic liquids do not boil. Instead, they decompose when reaching temperatures between 300° C and 400° C.
3. Surface Tension: Compared to liquid metals and other fuels, ionic liquids typically have lower surface tension. This is critical in electrospray applications, as lower surface tensions allow for lower onset voltages.
4. Bipolar operation: More specific to electrospray thrusters, ionic liquids can operate with either a positive or a negative applied voltage. Liquid metals are only capable of operating with positive applied voltages [19].

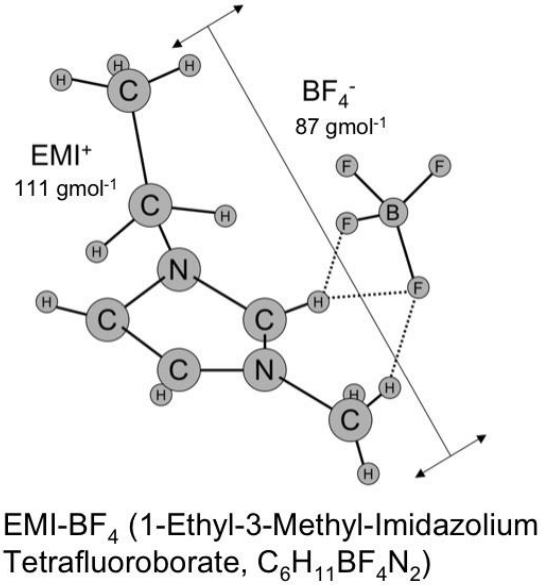

Figure 8: EMI-BF4 composition. [21]

Additionally, the number of species of ionic liquids far exceeds that of liquid metals, resulting in a near-limitless number of possible ion sources. Currently there are approximately 1000 different ionic liquids. In regards to electrospray thrusters, only a handful have been studied with the aforementioned EMI-BF_4 being one of the best performers. Table 1 provides a comparison of surface tension and conductivity values between fuels that have been used in electrospray thruster applications.

One drawback to ionic liquids is that operating in one polarity for extended periods results in buildup of the opposite polarity ion on the emitter surface. This causes degradation of the emitter surface leading to reduced efficiency. Lozano et al. performed experiments alternating polarity of applied voltages, and found that alternating the polarity at a rate of 1 Hz reduces the charge buildup, extending the life of the thruster. After 220 hours of continuous emission, no signs of degradation were observed [22].

Table 1: Surface Tension and Conductivity of Commonly Used Ion Sources.

Liquid	Surface Tension, γ (dyne/cm)	Electrical Conductivity, K (S/m)
Gallium	711[19]	7.1*10^6
Glycerol	63 (20 °C)	<0.1[3]
Formamide	58.3 (20 °C)[23]	1.5-2.9[16]
Tributyl Phosphate	27.2[24]	0.0085-0.33 (22 °C)[16]
EMI-Im	41[25]	1.01 (24 °C)[16]
EMI-BF_4	52[19]	2.3 (50 °C)[19]
	54.4[26]	1.36 (25 °C)[26]

Additionally, the presence of Fluorine in EMI-BF_4 requires outgassing of the propellant's surroundings to eliminate any water vapor. Fluorine is known to be highly reactive, and the presence of water vapor will cause Fluorine to react with the hydrogen and form hydrofluoric acid [27].

2.4: Field Evaporation and the Purely Ionic Regime

When working with an ionic liquid and at sufficiently high enough electric fields, an electrospray thruster will emit in what is referred to as the "Purely Ionic Regime" (PIR). The PIR gets its name from the fact that the electrospray emits particles as ions instead of particle droplets or a mixture of droplets and ions. Due to the much lower particle mass compared to droplet emission, the thrust from a PIR thruster will be lower; however, particles are emitted at much higher speeds, resulting in higher Isp.

This purely ionic emission can be represented as an activated process [21], in which case the current density can be expressed as,

$$j = \sigma \frac{kT}{h} e^{\left[-\frac{\Delta G}{kT}\right]} \tag{27}$$

where *k* and *h* are Boltzmann's and Planck's constants, respectively, and ΔG is the free energy of solvation. The value of ΔG is for a specific type of ion, and is on the order of 2 eV for many solvated ions [21]. Equation (27) highlights the need for an electric field in order for emission, as without one temperatures in excess of 1000° C would be necessary. Not only would an ionic liquid not survive such an environment, it would also be impractical to put one in such a small area defined by a CubeSat.

A 1D model can be used to show the forces acting on a charge, *q*, outside the liquid-vacuum interface. See Figure 9. The repelling force from the applied field, $F_E = qE$, and an "image" charge of $-q$ at position $-x$, $F_I = \frac{-q^2}{4\pi\varepsilon_0(2x)^2}$, both act on the ion. Bringing the particle to its given location from the surface requires an amount of work given by the equation [21],

$$W = \int_{\infty}^{x} (F_E + F_I)\, dx = \int_{\infty}^{x} qE\, dx - \int_{\infty}^{x} \frac{q^2}{4\pi\varepsilon_0(2x)^2}\, dx \tag{28}$$

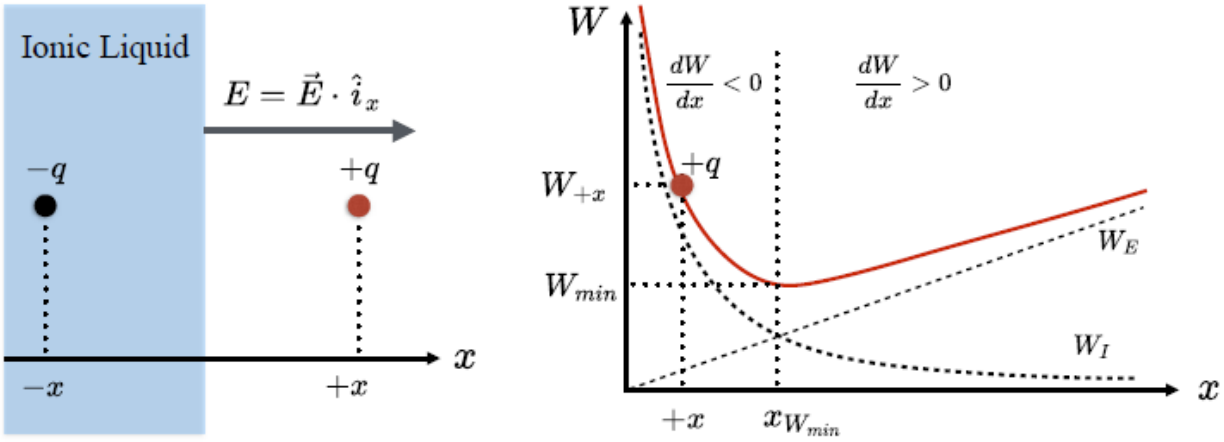

Figure 9: 1D representation of forces and work on a single charge at ionic liquid-vacuum interface. [21]

With the electric field *E* disappearing at infinity, equation (28) integrates to,

$$W = W_E + W_I = qEx + \frac{q^2}{16\pi\varepsilon_0 x} \tag{29}$$

Work will be minimum at some distance from the interface, $x = x_{Wmin}$. Without an applied electric field, *dW/dx < 0*, resulting in a negative force acting on the particle that attracts it to the interface. Assuming the distance *+x* is on the order of the dimension of a molecular ion, then the work required to bring a particle from *+x* to ∞ can be approximated as $W_{+x} \approx \Delta G$. With an applied electric field, a charged particle no longer needs to be moved to infinity. Instead, it only needs to travel some distance $\Delta x = x_{Wmin} - (+x)$ in order to escape. With *dW/dx > 0* to the right of minimum, a positive force pushed the particle away from the interface. The result is a reduction in required energy for evaporation. This reduced energy can be expressed as $\Delta G - W_{min}$, where W_{min} can be determined by setting the derivative of equation (28) to zero, and solving for x_{Wmin} [21],

$$x_{Wmin} = \left(\frac{q}{16\pi\varepsilon_0 E}\right)^{1/2} \tag{30}$$

Substituting equation (30) back in to equation (28), W_{min} becomes,

$$W_{min} = \left(\frac{q^3 E}{4\pi\varepsilon_0}\right)^{1/2} \equiv G(E) \tag{31}$$

The term *G(E)* represents the reduction of free energy as a result of the applied normal field, *E*. From this, the field-evaporated current emitted per unit area can be found. The result was derived by Iribarne and Thompson [28], a full derivation of which can be found in the reference material, and is given by,

$$j = \sigma \frac{kT}{h} e^{\left[-\frac{\Delta G - G(E)}{kT}\right]} \tag{32}$$

2.4.1 Emission in PIR

One major difference when operating in the PIR is that no jet forms from the Taylor Cone. Instead, a closed surface is formed with radius R^* at the apex. Since the evaporation rate defined by equation (32) is highly sensitive to the value of $G(E)$, there should exist a critical field at which ion emission begins to occur. This critical field, called E^*, has a value that results in $G(E^*) \approx \Delta G$ [21],

$$E^* \approx \frac{4\pi\varepsilon_0}{q^3}\Delta G^2 \tag{33}$$

The liquid surface is at equilibrium, thus electrostatic stresses and surface tension must balance each other,

$$\frac{1}{2}\varepsilon_0 E^{*2} - \frac{1}{2}\varepsilon_0 E_{in}^2 = \frac{2\gamma}{R^*} \tag{34}$$

where E_{in} is the electric field inside the liquid which has the approximate value E^*/ε, with ε being the relative permittivity of the liquid. The relative permittivity, ε, is defined as the ratio of the substance permittivity to the permittivity of free space. Rearranging to solve for R^*,

$$R^* \approx \frac{4\gamma}{\varepsilon_0 E^{*2}}\left(\frac{\varepsilon}{\varepsilon - 1}\right) \tag{35}$$

Ions must reach the surface to evaporate, and do so at a rate j,

$$j = KE_{in} \approx K\frac{E^*}{\varepsilon} \tag{36}$$

where K is the electrical conductivity. This is the same j in equation (32) and because of this and the exponential relation of equation (32), equation (36) regulates emissions in order for j to be equal in both. Field evaporated current from a hemispherical meniscus apex of radius R^* is defined as [21],

$$I \approx \frac{32\pi K\gamma^2}{\varepsilon_0^2 E^{*3}} \frac{\varepsilon}{(\varepsilon-1)^2} \tag{37}$$

The resulting thrust density becomes,

$$\frac{T}{A} = \frac{1}{2}\varepsilon_0 E^{*2}\left(\frac{\varepsilon-1}{\varepsilon}\right) \tag{38}$$

For the values of K and γ for EMI-BF_4 in Table 1, and a critical field value of E^* = 1.5 x 10^9 V/m, the emitted current is on the order of 154 nA. The thrust will be quite low, approximately 10 μN; however the thrust density approaches 10^7 N/m^2, demonstrating the value in having multiple compact thrusters clustered together to achieve more reasonable thrust levels [21].

2.5: Field Enhancement Factor

An important parameter in defining how effective a set of emitters is at increasing the electric field is the field enhancement factor, β. In simplest terms, it is the ratio of the field at the emitter tip to the applied field. As emitters are brought closer together in an array, the electric fields of individual emitters begin to interfere with one another, reducing overall field strength. This is often called shielding or screening. Because the emitter tip field strength decreases, shielding effects result in a drop in enhancement factor. Reduced field strengths will also result in reduced performance of the electrospray thruster. Determining the optimal emitter spacing is thus an important factor in achieving high field enhancement factors.

Research performed by Harris et al. on determining optimal spacing found that the enhancement factor of a single emitter in isolation, β_0, serves as an asymptote for β [29]. Increasing the emitter spacing, b, results in an increase in β until β approximately

equals β_0, at which point β remains constant as b increases. Thus, there must exist a minimum spacing, b_{opt}, at which β approximates β_0, and above which β no longer increases. The field enhancement factor as a function of spacing is given below,

$$\beta(b) = \beta_0 \left[1 - e^{\left(a\left[\frac{b}{h}\right]^c\right)}\right] \tag{39}$$

Here, a is a constant, c is a constant dependent on array configuration, and h is the emitter height. The authors note that while many groups have adopted a form of equation (39) without the term c in the exponent, results using this equation match well with their Line-Charge Model (LCM) results, thus this form will be used. The current density of an array can be found using a modified Fowler-Nordheim equation,

$$J_{array}(b) = \left[\frac{k}{b^2}\right][2\pi r_T^2]\left[\frac{1}{\frac{B\phi^{3/2}}{\beta(b)E_0} - \nu + 1}\right]\frac{A}{\phi t_0^2}\left(\frac{\phi^2 e^6}{4Q}\right)^{\nu}(\beta(b)E_0)^{2-\nu}e^{\left(-B\frac{\phi^{3/2}}{\beta(b)E_0}\right)} \tag{40}$$

The first bracketed term on the right-hand side of equation (40) defines emitter density with k depending on the configuration. The second term gives the current emitted by a single emitter of tip radius r_T, and is modified by the third bracketed term, which is defined as the geometry term, g. The remainder of equation (40) is the normal Fowler-Nordheim equation. B is a constant equal to 6.8309 nm^{-1} $eV^{-1/2}$, E_0 is the background field, and ϕ and ν are material-dependent properties.

Deriving equation (40) with respect to b and equating to zero results in,

$$\left.\frac{d\beta}{db}\right|_{opt} = \frac{2\beta(b_{opt})}{b_{opt}}\left[(g+1)\frac{B\phi^{3/2}}{\beta(b_{opt})E_0} + 2 - \nu\right]^{-1} \tag{41}$$

Harris et al. note that while equation (41) appears to define $d\beta/db$, it actually does not due to it being derived from equation (40), which does not take shielding effects into

account [29]. Thus, equation (41) is a condition that must be met. Equations (39-41) clearly show how many parameters affect optimal emitter spacing. Combining equations (39) and (41) would allow one to solve for the optimal spacing; however, doing so results in a transcendental equation that requires a root solver.

Harris et al. compared results using the above procedure with results from Line Charge Model calculations for emitters with a 1.5 μm radius and 1500 μm high in both square and triangular arrays [29]. They found that optimal spacing decreased from 6000 μm at an applied field of near zero MV/m, to below 1500 μm at a field of 300 MV/m. Their results matched Line Charge Model calculations to within 1% for a = -1.265, and c = 1.09 for the triangular array, and a = -1.45, and c = 1.09 for the square array [29].

Chapter 3: Model Setup

3.1: Cone Model

All models and simulations were built within ANSYS's Electronics Desktop (EDT) Electromagnetic Suite and solutions were performed using the Maxwell3D solver within ANSYS EDT version 19.0. For simplicity in design and to help reduce solution time, the needles were modeled as a cone with a hemispherical tip. Measurements taken by Dr. Costa et al. at the CLA indicated a needle base-to-tip height of 6 μm, base diameter of 0.5 μm, and tip diameter of 0.2 μm. Using Maxwell3D's built-in modeler, a single needle was modeled using a cone at the origin with a base radius of 0.25 μm, top radius of 0.1 μm, height of 5.9 μm, and a 0.1 μm radius sphere centered at a height of 5.9 μm. The two objects were then combined to create the needle profile. An example is provided in Figure 10. This needle was then duplicated using the modeler's "Duplicate" command to create an array of needles.

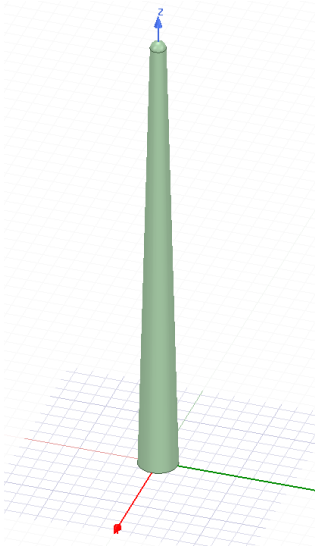

Figure 10: Needle geometry used in simulations.

An attempt at modelling a prolate spheroid geometry tip was made using an ellipse revolved around the z-axis. From Figure 3, the tip height was estimated to be 0.5 µm. The needle geometry was then sketched in SolidWorks 2017 to determine the ellipse center. The line forming the edge of the cone was set tangent to the ellipse, which was trimmed using the Trim tool to form the needle tip shape. The point at which the tangent line meets the ellipse was set to 0.5 µm from the tip and a height of 0.1 µm. The center point and radii were then found by dimensioning their respective points. See Figure 11.

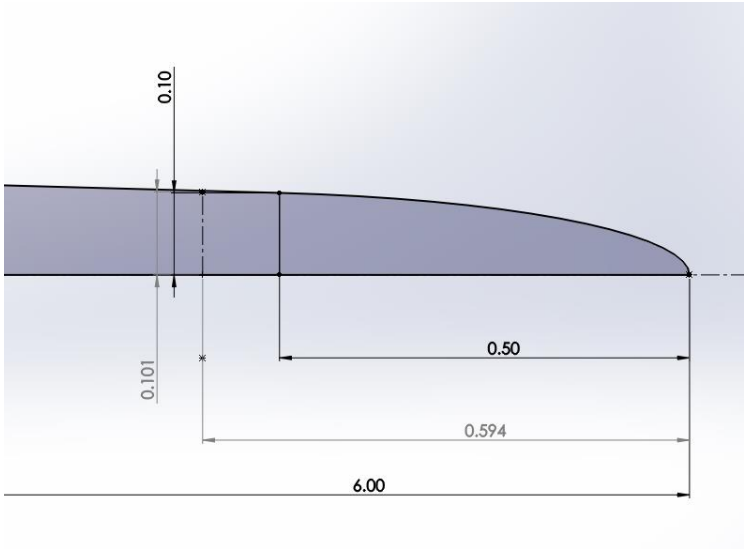

Figure 11: SolidWorks sketch of ellipse geometry.

These points were then used to generate an ellipse in ANSYS EDT that was cut along the YZ plane, revolved 360° around the z-axis, and then combined with the cone to form the sharp-tip needle. See Figure 12. This procedure was done in order to ensure smooth transition between the cone and ellipse shapes when combined in ANSYS EDT.

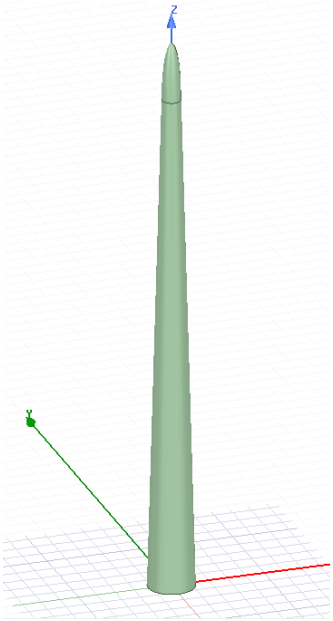

Figure 12: Sharp-tip needle geometry in ANSYS.

3.2: Boundary Region

ANSYS EDT requires models to have a defined solution region that encloses the geometry used in the solution, which is assigned the “vacuum” material. The chosen solver will only find solutions within this region; anything outside will be ignored or result in an error. The base size is based on work performed by Harris et al on shielding effects in ungated emitter arrays [29]. In their work, they define a “local area” outside of which shielding effects on the central emitter are negligible. The size of the local area depends on emitter spacing, and also the configuration used, either square or triangular. Shown in Figure 13, the radii specifying local area for square and triangular arrays, respectively, are giving by $\frac{4}{\sqrt{2}}b$ and $3b$, where b is the emitter spacing.

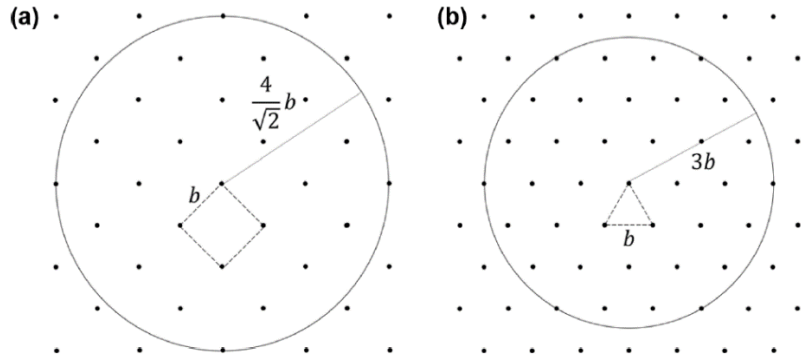

Figure 13: Boundary region size for (a) square and (b) triangular Arrays. [29]

While the reference defines the bounding region as a circle, the mesh for needles along the curved edge of a cylindrical boundary region failed to generate properly. Element nodes were not mapped along the surface of the needle tip, shown in Figure 14. This prevented the software from solving for the electric field across most of the tip, and instead produced a result of zero. A box region was chosen instead since the added area is outside the region defined by a normally circular area, thus it should have minimal effects on results.

The height of the boundary region was used to represent the extractor grid spacing, with the plane opposite the needles acting as the extractor grid. While there is no relation between needle pitch and grid spacing, the equations in Section 2.1 show that grid spacing does affect electric field strength. The presence of field enhancers further complicates the relation.

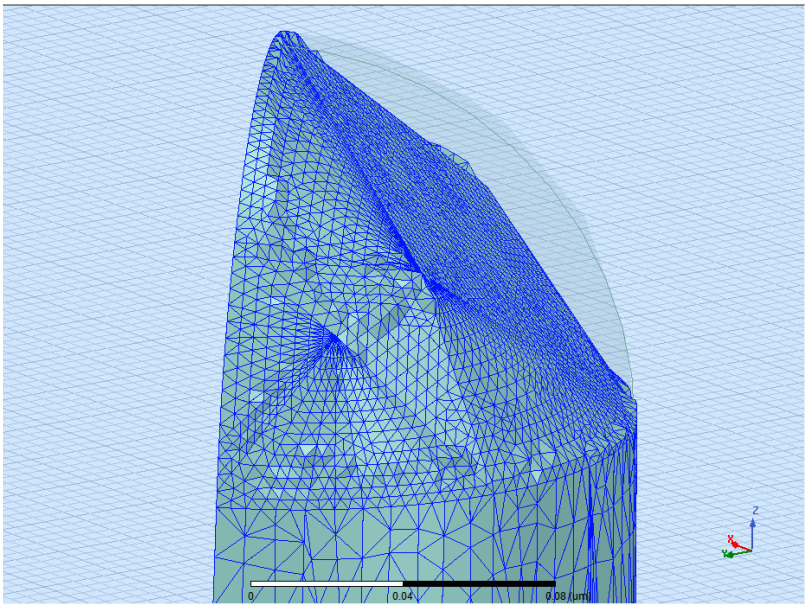

Figure 14: Sample of failed mesh generation along curved boundary

Several authors who have performed electrospray thruster experiments have used a variety of grid spacings, achieving different starting voltages [6], [11], [30], [31], [32], [33], [34], [35]. Table 2 provides extractor spacing values, along with data for emitter type, geometry, pitch, and applied voltage from previous experiments, and these values were compared to determine a suitable spacing to use. The negative extractor grid spacing values from Courtney et al. indicate that the emitters extend into the holes of the grid, causing the grid face to be below the emitter tip.

Table 2: Previous Electrospray Thruster Details.

Research Group	Emitter Type	Extractor Spacing	Emitter Pitch	Emitter Diam.	Emitter Height	Propellant	Voltage
Alexander [31]	Capillary	3-4 mm	267 μm	36-560 μm OD, 25-305 μm ID	400 μm	NaI-doped Tri-Ethylene-Glycol	Varied, up to 9.25 kV
Courtney (MIT) [32]	Ext. "Volcano"	125±20 μm	450 μm	15-30 μm	150-170 μm	EMI-Im	1000-2500
	Ext. Rounded	125±20 μm	450 μm	5-20 μm	150-170 μm	EMI-Im	750-1500
	Ext. Rounded	140±25 μm	450 μm	5-20 μm	150-170 μm	EMI-BF_4	1125
Courtney, Dandavino, Shea (EPFL) [35]	Linear, Triangular Prism	-20±20 μm	0.8 mm	20 μm	320 μm	EMI-Im	1550
		-50±30 μm			315 μm	EMI-Im	1550
		105±30 μm			285 μm	EMI-BF_4	2100
Dandavino [11]	Capillary	50 μm	670 μm	45 μm OD, 5 μm ID	70 μm	EMI-BF_4	1000 w/up to 3000 accel.
Krpoun, Shea [33]	Capillary	90 μm	250 μm	44 μm, 34 μm tip, 24 μm ID	70 μm	EMI-Tf2N	1200
Krpoun, R [30]	Capillary	25 μm	250 μm	20 μm ID	70 μm	EMI-BF_4	700
		40 μm					720
Velásquez-García [6]	Ext. "Pencil"	250 μm	200 μm	50 μm, 3 μm tip	270 μm	EMI-BF_4	0-3250
	Ext. "Volcano"	250 μm	200 μm	90 μm, 6 μm rad. curve	270 μm	EMI-BF_4	
Velásquez-García [34]	Flat Rect.	350 μm	130 μm	12 μm	15 mm	NaI-doped Formamide	2500

A tip-to-extractor distance of 40 μm was ultimately chosen due to its displayed lower starting voltages, and because it results in a more compact thruster compared with most other designs. Although tests have been performed with 25 μm extractor spacing [30], which would certainly allow for an even more compact design, these tests use much longer emitters- resulting in a larger overall thruster height. With much shorter emitters and overall smaller thruster design, ease of manufacturing is a concern with such small distances.

3.3: Configurations

Several different arrangements were modeled to simulate different configurations. The first configuration is a “full” 5 x 5 array (Figure 15) that was run for comparison with the symmetric array. The 5 x 5 size was chosen as it is the maximum number of needles that fit within the specified boundary region.

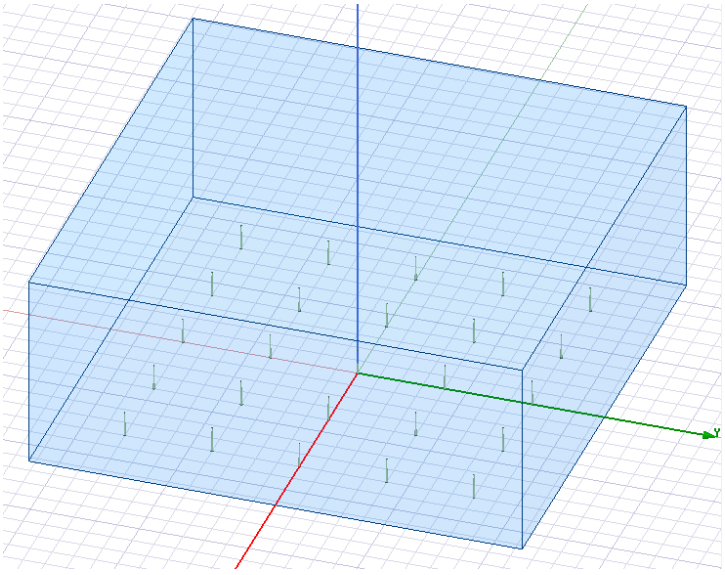

Figure 15: Full 5 x 5 needle array.

The symmetric array (Figure 16) consists of only a ¼ section of the full array cut along the XZ and YZ planes. These two configurations were compared to determine the accuracy of the symmetric array, as it is preferable to run simulations using a symmetrical model since a smaller model requires less computational time.

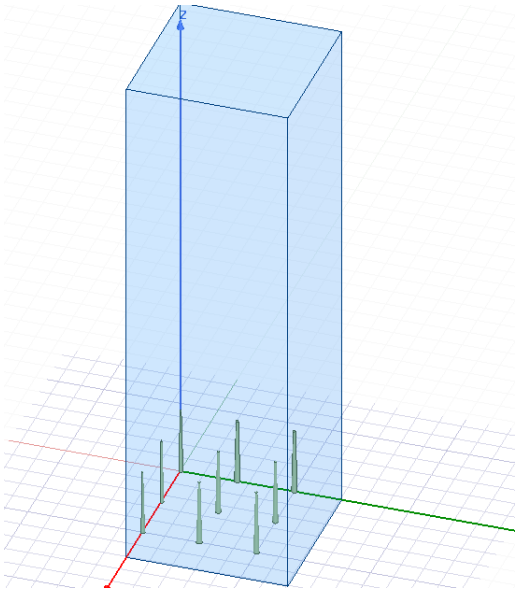

Figure 16: Symmetrical square array.

A single needle configuration was run to determine the field enhancement factor, β, of a single needle. A triangular configuration modeled according to Figure 13b was compared with the square array. Finally, a single needle with an elliptical “sharp” tip was simulated to compare field strength with the spherical tip geometry. Simulations of a square array of these sharp-tip needles were run; however, they failed to finish, with ANSYS stating memory space errors. Results for each case are discussed in Chapter 4.

3.4: Simulation Parameters

An electric field of 1.5 x 10^9 V/m was assumed in order to reach purely ionic conditions. PIR has been stated to start as low as 1 x 10^9 V/m [16], however 1.5 x 10^9 V/m provides a more conservative result to help ensure the PIR assumption stands. With this field value, an extractor spacing of 40 μm, EMI-BF_4 propellant, and a prolate spheroid geometry with a radius of curvature of 0.1 μm, solving equation (23) for voltage yields 553.33 V. Equation (23) instead of (25) was used since a particular field strength is necessary, and equation (25) only provides the voltage required for general ion emission, not PIR emission. Solving equation (25) and substituting into (23) gives a starting voltage of 182.2 V and a field of 4.9392 x 10^8 V/m, which is not strong enough for PIR emission. It is, however, strong enough to induce droplet emission.

In each simulation 553.33 V is applied to the needles and bottom face of the boundary region, and a voltage of 0 V is applied to the top face representing “ground” at the extraction grid.

For the symmetric cases, the symmetry boundary condition is applied to the faces of the boundary region along the XZ and YZ planes. An initial needle spacing value of 5 μm was evaluated for all cases. For all but the single needle cases, the spacing was then set to vary from 10 μm to100 μm at 10 μm increments. This range was chosen to determine if the optimal spacing would fall within a range much smaller, sometimes by an order of magnitude, than existing electrospray thrusters. A range from 125 μm to 200 μm at 25 μm increments was run for the symmetric arrays to compare results with the lower end of ranges found in other electrospray thruster experiments.

3.5 Mesh Refinement

ANSYS EDT uses an adaptive refinement process to generate and solve meshes. After specifying initial mesh properties, the mesh is then refined by a defined percentage, and the new solution is calculated. If the results are within specified error conditions, the simulation ends. If not, the mesh is refined further and solved again. The initial mesh can be defined using a relative slider, or manually. Further mesh operations such as size limits can be assigned as necessary. Initial simulations used a mesh with the relative slider set to the finest value. When running symmetrical cases, the mesh of needle tips along the boundary at spacing values 20 μm and above failed to generate in a manner similar to what was described in Section 3.2, and shown in Figure 14. This problem persisted even after adding a length-based restriction of 0.005 μm to the tip region.

The initial mesh settings were set to manual control, where the following values can be adjusted: surface deviation, normal deviation, and aspect ratio. Surface deviation measures the distance from the true surface to the element face, normal deviation measures the angle between the mesh surface and a line perpendicular to the curve, and the aspect ratio is the height to width ratio of the element. Using a surface deviation of 0.005 μm, normal deviation of 17°, and aspect ratio of four produced continuous results for spacings up to 90 μm in the square array. Changing the normal deviation to 15° produced continuous results for the 100 μm spacing. Simulations for the triangular array used the same settings as the square array; however, a normal deviation of five degrees was needed for 70 μm to 100 μm spacings. For the sharp-tip needle, the surface deviation remained the same while the normal deviation and aspect

ratio were set to five degrees and 4.5, respectively. Tighter surface deviation and looser aspect ratio were required for the 125 μm to 200 μm spacings in both square and triangular configurations. These were set to 0.001 μm and 1.2, respectively, with a normal deviation of five degrees. The results are discussed further in Chapter 4.

The defined percentage for mesh refinement mentioned above was kept at the default value of 30%. Solutions converged after two refinement passes regardless of configuration, and minimal improvement was found after experimenting with a single needle configuration, so long as a fine mesh was used. Table 3 shows single needle results at different mesh settings using both relative slider values, and manual settings.

Table 3: Mesh Refinement Comparison.

Slider Value	Refinement Percentage	Field Strength (x10 V/m)	% Change	# of Tetrahedra
1 "coarse"	30	5.1869		58522
5 "medium"	30	5.8195	12.1961%	101393
9 "fine"	30	5.8118	-0.1323%	117396
	100	5.84	0.4829%	170526
Manual	30	5.8327	-0.1252%	92068
	100	5.8032	-0.5083%	122875

The manual cases used the first settings mentioned above. It is clear from these results that so long as a “medium” or finer mesh is used, there is little change in results. The manual settings defined above equate to a relative slider value of “9,” the finest setting, when using the “Convert to Slider” function. When solving the needle arrays, such small changes in results are not worth the added computation time, particularly at large spacings. Thus, the decision was made to keep the refinement percentage at the default value of 30%.

3.6: Field Enhancement Factor Calculations

Field enhancement factors were calculated for various values of b in equation (39). These results were compared with the field enhancement factor based on results from simulations, and are discussed in Chapter 4. Based on results from Harris et al. the values for a and c in equation (34) are defined as -1.45 and 1, respectively, for a square array, and -1.265 and 1.09, respectively, for a triangular array [29]. The resulting background field, E_0, from a voltage of 553.33 V and total distance of 46 μm is 1.2029 x 10^7 V/m, and was used to find β_0 once the single needle cases were run. Finally, h in equation (34) is the emitter height of six μm.

Chapter 4: Results and Discussion

4.1: Single Needle

Figure 17 plots the electric field magnitude along an arc covering the curvature of the needle tip. The maximum value was found to be 5.8126 x 10^8 V/m. This value is much lower than the 1.5 x 10^9 V/m required for PIR, which was used to calculate the applied voltage in the simulation. The difference is expected due to the needle being modeled as a spherical tip as opposed to a prolate spheroid that is assumed in equation (25); however, since all needles use the same geometry and exhibit the same result trends, these results are still valid for comparison purposes.

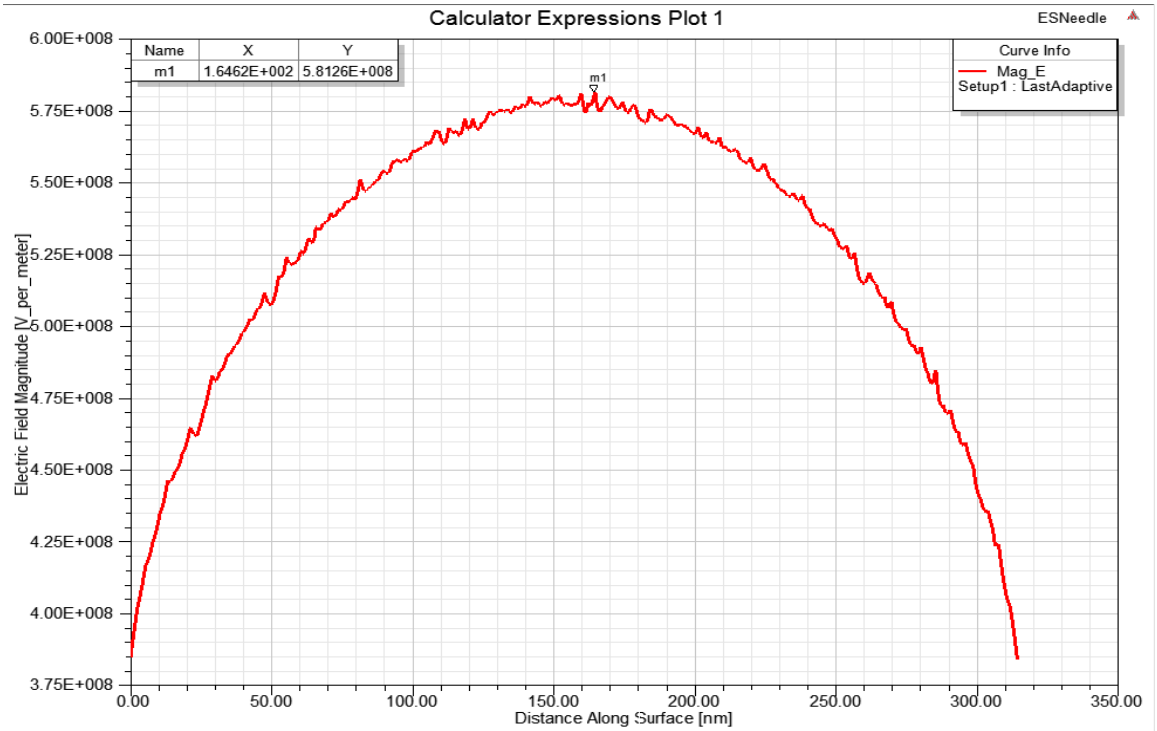

Figure 17: Electric field magnitude for a single needle.

The wave-like features along the curve in Figure 17 are likely due to the non-uniformity in the tip mesh grid. Result plots from mesh refinement comparisons in Section 3.5 showed that these features did smooth out with finer meshes; however, they did not disappear entirely. This indicates adjustments to initial mesh settings and better refinement are needed to achieve a uniform mesh and smooth plot. Since these features appear in all simulations and exhibit the same trends, the error compared to a smooth curve should be relatively equal throughout the results. Thus, the results presented are still valid for comparison purposes.

4.2: Full Array vs. Symmetric Array

Table 4 lists the maximum field magnitude values for the full 5 x 5 array and the square symmetric array for needle spacings of 5 μm and 10 μm to 100 μm. These measurements were taken at the center needle, and the needle at the corner of the array. The corner needle was chosen since it is the furthest from the center and has the fewest needles surrounding it. Therefore it experiences the least amount of shielding, more closely resembling the case of a single needle. Results from the closest spacing show a stronger field at the corner needle. While there is a large difference from the single needle value due to shielding, it is closer than that of the center needle indicating the corner experiences less shielding. Thus when both corner and center needles emit fields of the same strength, shielding is no longer present.

The “% Difference” columns show the percent difference in field magnitude between the two configurations for a given spacing and needle position. From these

values it can be seen there is very little difference when using a symmetric array over the full array, thus validating the use of a symmetric model.

Figure 18 and Figure 19 display the field magnitude plots for the full array, providing a visualization of field strength trends. Figure 19 only covers a 90° arc due to the center needle being at the intersection of symmetry planes; however, from the two figures it is evident the trends are the same. Adjacent lines represent center and corner results for a given spacing, with the corner having a slightly stronger field and thus being the higher of the two. For example, the lowest two lines in Figure 18, the red and grey lines, are the center and corner results, respectively, from a five μm spacing. The next pair of lines, 10 μm spacing, and so-on. Note how above at 20 μm spacing and above, the plot lines appear to converge, and the maximum field magnitude no longer significantly increases. This indicates that the optimal needle spacing is approximately 20 μm.

Table 4: Maximum Field Magnitudes for Full and Square Symmetric Arrays.

	Full Array ($x10^8$ V/m)		Square Array ($x10^8$ V/m)		% Difference	
Spacing (μm)	Corner	Center	Corner	Center	Corner	Center
100	5.8951	5.8220	5.8199	5.8119	1.2756%	0.1735%
90	5.8386	5.8456	5.8386	5.8457	0.0000%	0.0017%
80	5.8551	5.8238	5.8239	5.8281	0.5329%	0.0738%
70	5.8311	5.8662	5.8640	5.8668	0.5642%	0.0102%
60	5.8292	5.8304	5.8642	5.8077	0.6004%	0.3893%
50	5.8423	5.8432	5.8467	5.8205	0.0753%	0.3885%
40	5.8548	5.8561	5.8616	5.8488	0.1161%	0.1247%
30	5.8757	5.8483	5.8399	5.8048	0.6093%	0.7438%
20	5.7541	5.7770	5.8252	5.7325	1.2356%	0.7703%
10	5.4105	5.2452	5.4598	5.2317	0.9112%	0.2574%
5	4.1546	3.7986	4.1618	3.7551	0.1733%	1.1452%

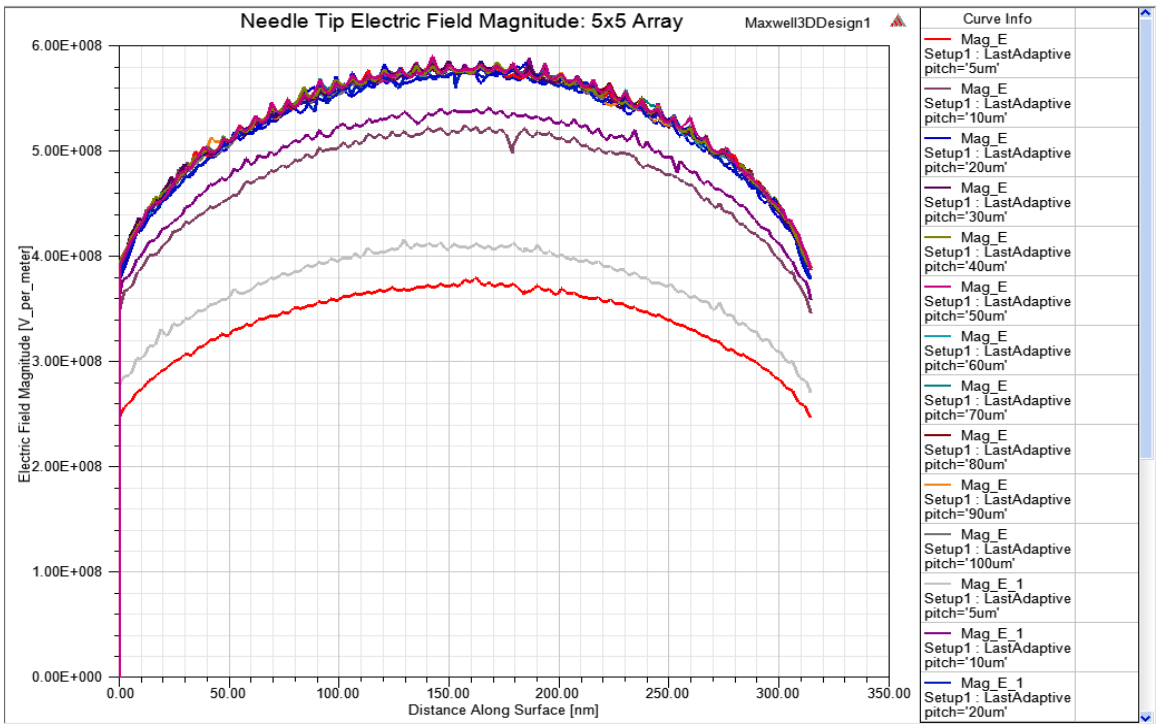

Figure 18: Full array field magnitude plots.

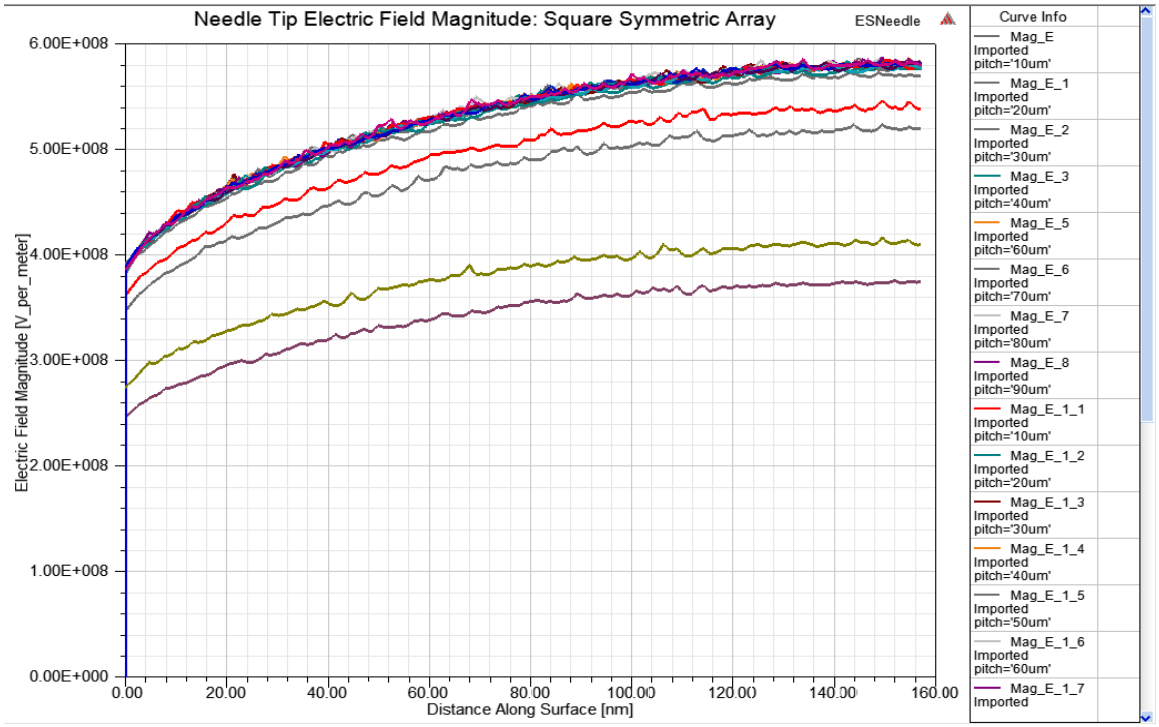

Figure 19: Square symmetrical array field magnitudes

4.3: Square Array

Figure 20 duplicates Figure 19, but also includes results from the 125 μm to 200 μm spacing simulations. Even at higher spacings, the electric field shows no significant increase in magnitude, approaching an asymptotic value of approximately 5.9 x 10^8 V/m. Table 5 includes maximum field values for the additional spacing simulations.

Electric field values for previous thrusters listed in Table 2 are rarely given, making comparison difficult for emitter pitches near 200 μm. Using emitter information provided from Velasquez-Garcia [6], which uses an emitter pitch of 200 μm, the estimated electric field at the tip using equation (24) is 3.7297 x 10^8 V/m for a voltage of 3250 V. It can be seen from Figure 5e of Reference [6] that the “pencil” type emitter used appears much sharper than the prolate spheroid assumed from equation (24). From this, and the mention of tips ejecting ions, it can be assumed the tip field values are much closer to the 1 x 10^9 V/m needed for ion emission. The other data of interest to compare to is that of the externally wetted, round tip emitters tested by Courtney [32], who initially estimated electric fields of 0.1 to 0.6 x 10^9 V/m at 1100 V. While the design has much larger emitter spacing than examined in this research (450 μm), it has been developed into MIT’s Scalable ion Electrospray Propulsion System (S-iEPS) [36, 37], allowing for comparison to an established electrospray thruster. Simulation results fall within the stated estimate; however, actual field results are not explicitly stated in Reference [32] and given that the S-iEPS thruster performs in the PIR regime [37], these field results are likely on the order of 1 x 10^9 V/m.

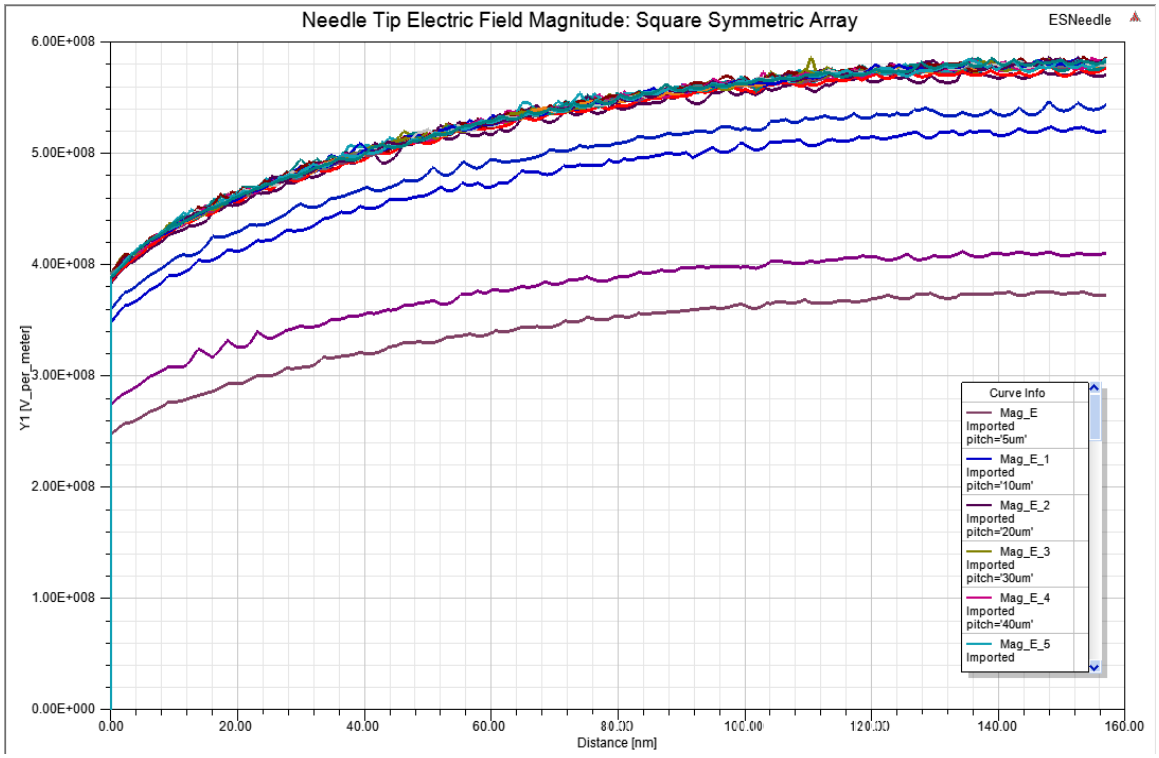

Figure 20: Square array field magnitudes including 125 µm to 200 µm results.

Table 5: Complete Square Symmetrical Array Field Magnitude Results.

	Square Array Maximum Field Magnitudes (x10^8 V/m)	
Spacing (µm)	Corner	Center
200	5.8530	5.8292
175	5.8498	5.8143
150	5.8361	5.8275
125	5.8361	5.8326
100	5.8199	5.8119
90	5.8386	5.8457
80	5.8239	5.8281
70	5.8640	5.8668
60	5.8642	5.8077
50	5.8467	5.8205
40	5.8616	5.8488
30	5.8399	5.8048
20	5.8252	5.7325
10	5.4598	5.2317
5	4.1618	3.7551

4.4: Triangular Array

Figure 21 contains plots of the triangular array results, while Table 6 provides maximum field magnitude values. These results display the same pattern as previous results, indicating that shielding effects stop once the needle spacing reaches 20 μm. The percent difference from the square array is also provided in Table 6. Ref [29] mentions that stronger shielding should be present in a triangular array, evident by smaller field magnitudes. While this is certainly the case at low needle spacings, results indicate little difference between square and triangular arrays at higher spacings; including only a 1.39% difference at 20 μm where shielding begins to stop. This discrepancy with the literature may be due to differences in needle geometry.

Table 6: Triangular Array Field Magnitude Results and Comparison.

	Triangular Array (x10^8 V/m)		% Difference from Square Array	
Spacing (μm)	Corner	Center	Corner	Center
200	5.8362	5.8459	-0.2870%	0.2865%
175	5.8242	5.8177	-0.4376%	0.0585%
150	5.8313	5.8093	-0.0822%	-0.3123%
125	5.8427	5.8469	0.1131%	0.2452%
100	5.8454	5.8181	0.4382%	0.1067%
90	5.8269	5.8396	-0.2004%	-0.1044%
80	5.8557	5.8223	0.5460%	-0.0995%
70	5.8444	5.8180	-0.3342%	-0.8318%
60	5.8779	5.8298	0.2336%	0.3805%
50	5.8541	5.8290	0.1266%	0.1460%
40	5.8394	5.8156	-0.3787%	-0.5676%
30	5.8340	5.8394	-0.1010%	0.5961%
20	5.7443	5.7029	-1.3888%	-0.5164%
10	5.0688	5.0828	-7.1614%	-2.8461%
5	3.3968	3.4453	-18.3815%	-8.2501%

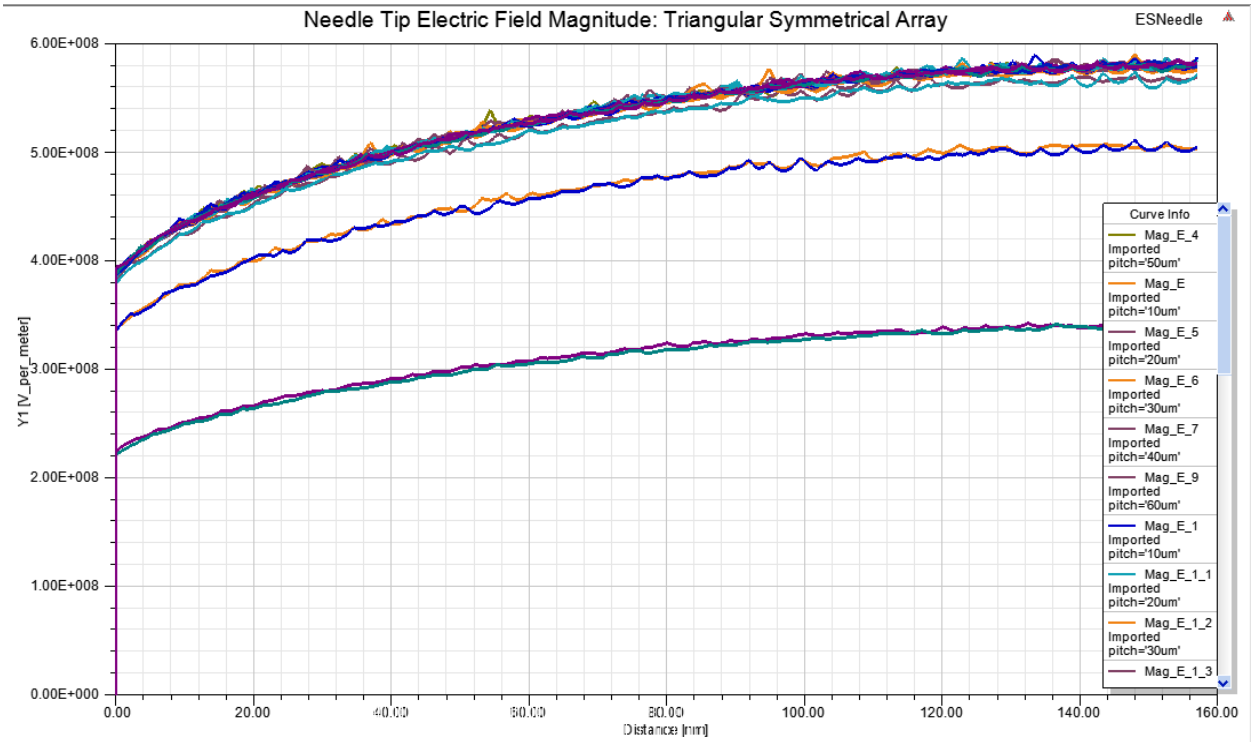

Figure 21: Triangular array field magnitudes.

4.5: Field Enhancement Factors

Using the maximum field magnitude of a single needle from Section 4.1 and the background field from Section 3.6, the single needle field enhancement factor, β_0, was found to be 48.37. This, along with the specified *a* and *c* values from Section 3.6, were used in equation (39) to find the enhancement factor as a function of spacing. The enhancement factors for the center and corner needles are found by taking the ratio of the simulated field and background field. Table 7 and Table 8 contain field enhancement factors for the square and triangular arrays, respectively, along with percent error from the calculated values.

Table 7: Square Array Field Enhancement Factors.

		Square Array		% Error	
Spacing (μm)	Calculated	Corner	Center	Corner	Center
200	48.3651	48.6574	48.4596	0.6943%	0.2849%
175	48.3651	48.6308	48.3357	0.6393%	0.0285%
150	48.3651	48.5169	48.4454	0.4036%	0.2556%
125	48.3651	48.5169	48.4878	0.4036%	0.3434%
100	48.3651	48.3822	48.3157	0.1249%	0.0128%
90	48.3651	48.5377	48.5967	0.4466%	0.5687%
80	48.3651	48.4155	48.4504	0.1937%	0.2659%
70	48.3651	48.7489	48.7721	0.8836%	0.9317%
60	48.3651	48.7505	48.2808	0.8870%	0.0850%
50	48.3649	48.6050	48.3872	0.5865%	0.1358%
40	48.3621	48.7289	48.6225	0.8487%	0.6284%
30	48.3308	48.5485	48.2567	0.5403%	0.0639%
20	47.9802	48.4263	48.2567	1.0202%	0.6664%
10	44.0501	45.3886	43.4924	3.1309%	1.1777%
5	33.9187	34.5981	31.2171	2.0941%	7.8828%

Table 8: Triangular Array Field Enhancement Factors.

		Triangular Symmetrical		% Error	
Spacing (μm)	Calculated	Corner	Center	Corner	Center
200	48.3651	48.5177	48.5984	0.4053%	0.5722%
175	48.3651	48.4180	48.3640	0.1988%	0.0870%
150	48.3651	48.4770	48.2941	0.3210%	0.0575%
125	48.3651	48.5718	48.6067	0.5171%	0.5894%
100	48.3651	48.5942	48.3673	0.5636%	0.0939%
90	48.3651	48.4404	48.5460	0.2453%	0.4638%
80	48.3651	48.6799	48.4022	0.7408%	0.1662%
70	48.3651	48.5859	48.3664	0.5464%	0.0922%
60	48.3651	48.8644	48.4645	1.1227%	0.8183%
50	48.3650	48.6666	49.4579	0.7135%	0.4288%
40	48.3629	48.5444	48.3465	0.4649%	0.4076%
30	48.3328	48.4995	48.5444	0.4346%	0.5275%
20	47.9249	47.7538	47.4096	0.2680%	0.9868%
10	43.0463	42.1382	42.2546	2.0221%	1.7515%
5	31.2191	28.2384	28.6416	9.4666%	8.1739%

It is clear for both arrays that simulated results show good agreement with the calculated values for spacings above 5 μm. Figure 22 and Figure 23 are presented for visual representation, with logarithmic horizontal axes. Both arrays exhibit the established pattern of field enhancement converging close to its maximum value around 20 μm, as do the calculated enhancement factors. LCM calculations in Ref [29] were performed with increasing spacing until the change in β was less than 2%. Adopting the same criteria, the data in Table 8 established the 20 μm spacing field values to which results have been converging around as the minimum spacing, since the change in β drops well below 2% when increasing spacing from 20 μm to 30 μm. While the change in β effectively reaches zero between 60 μm and 70 μm, indicating a minimum for spacing, the increase in enhancement factor is minimal and a denser array will provide higher current density, and thus high thrust density.

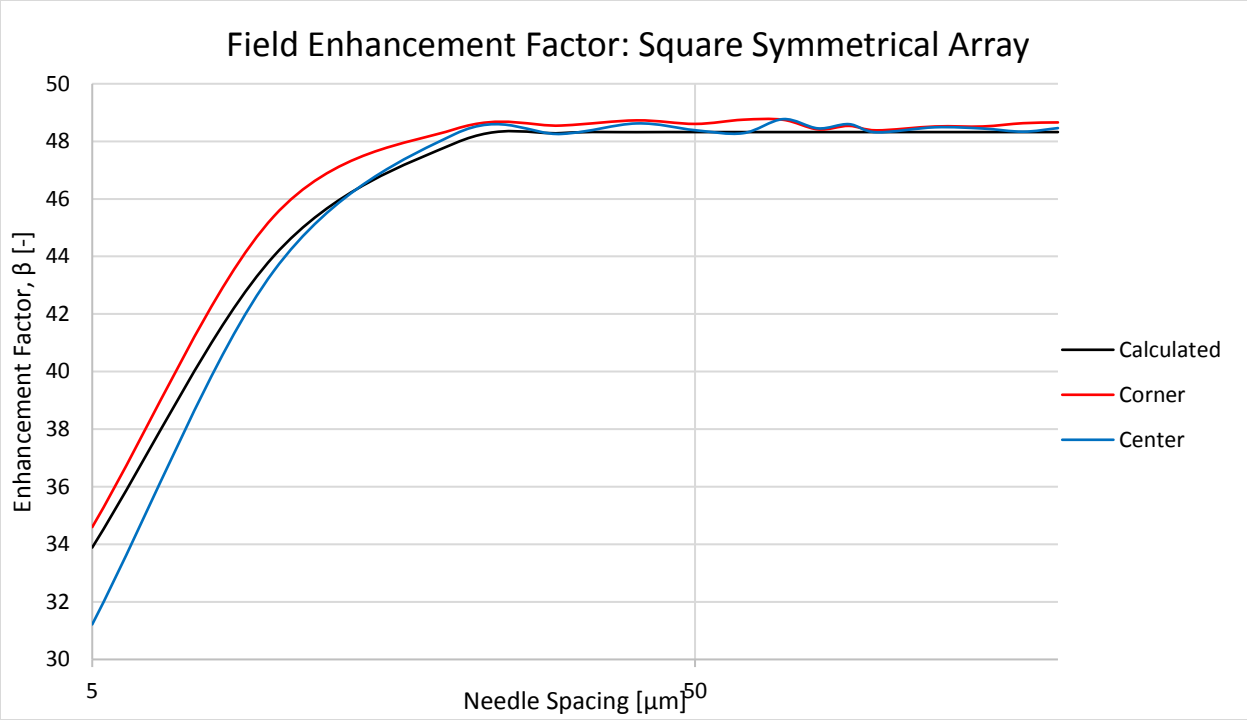

Figure 22: Square array field enhancement factor as function of spacing.

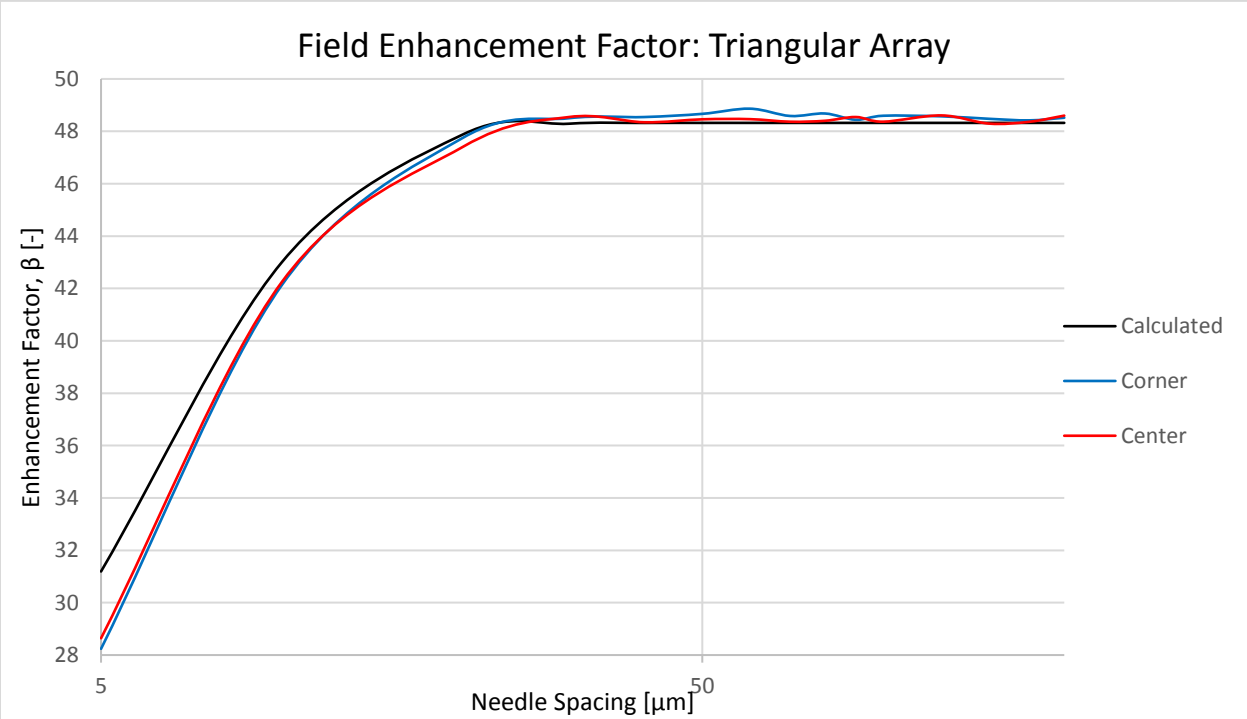

Figure 23: Triangular array field enhancement factor as function of spacing.

Table 9 provides calculations for the change in enhancement factor, *dβ*, for the calculated factors.

Table 9: Change in Calculated Enhancement Factor.

	β (-)		dβ (-)		% Change	
Spacing (μm)	Square	Triangular	Square	Triangular	Square	Triangular
200	48.3219	48.3219				
175	48.3219	48.3219	0.0000	0.0000	0.0000%	0.0000%
150	48.3219	48.3219	0.0000	0.0000	0.0000%	0.0000%
125	48.3219	48.3219	0.0000	0.0000	0.0000%	0.0000%
100	48.3219	48.3219	0.0000	0.0000	0.0000%	0.0000%
90	48.3219	48.3219	0.0000	0.0000	0.0000%	0.0000%
80	48.3219	48.3219	0.0000	0.0000	0.0000%	0.0000%
70	48.3219	48.3219	0.0000	0.0000	0.0000%	0.0000%
60	48.3219	48.3219	0.0000	0.0000	0.0000%	0.0000%
50	48.3216	48.3218	-0.0002	-0.0001	-0.0005%	-0.0003%
40	48.3188	48.3197	-0.0028	-0.0020	-0.0058%	-0.0042%
30	48.2876	48.2896	-0.0313	-0.0301	-0.0647%	-0.0623%
20	47.9373	47.8821	-0.3503	-0.4075	-0.7255%	-0.8440%
10	44.0107	43.0078	-3.9266	-4.8742	-8.1911%	-10.1797%
5	33.8884	31.1912	-10.1223	-11.8167	-22.9996%	-27.4756%

4.6: Sharp-Tip Needle

Figure 24 plots the field magnitude along the elliptical tip. Instead of gradually increasing over the tip curve as in the spherical tip, the field increases slowly until the radius quickly decreases to form a point. This results in a rapid increase in field strength near the tip of the needle, reaching an order of magnitude higher than the spherical tip. The discontinuity near the tip is a result of the mesh not mapping to the curved surface, as mentioned in Section 3.5. While this does bring the simulation results into question, the continuous nature of the curve up until that point indicates the results will remain valid upon further refinement. Additionally, the maximum field value of 1.6543×10^9 V/m is only 10.3% over the assumed value of 1.5×10^9 V/m used to

calculate the applied voltage. Taking a conservative approach by using the field value just prior to the discontinuity yields a magnitude of 1.5846 x 10^9 V/m, bringing the difference down to 5.64%. This indicates the 553.33 V potential calculated to generate an assumed electric field of 1.5 x 10^9 V/m is a good approximation. Since only the field enhancement factor of a single needle, β_0, changes in equation (39), it is reasonable to assume that an array of needles using this geometry would follow the same trends seen when using a spherical tip.

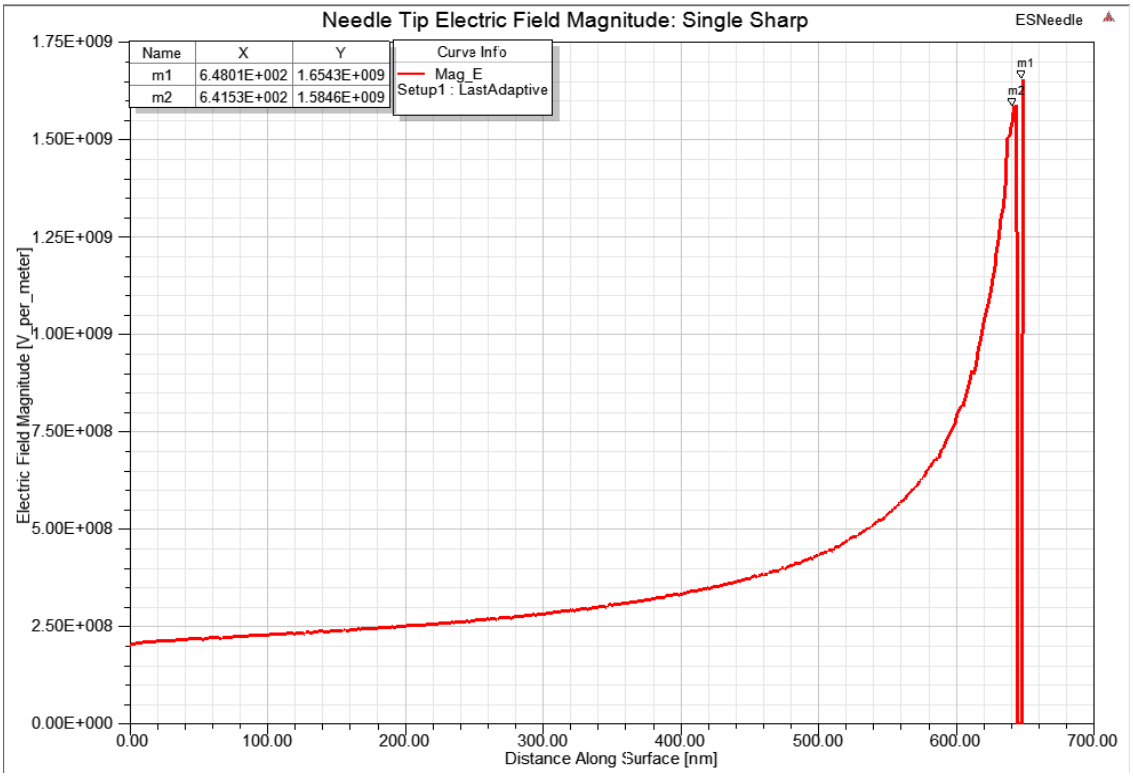

Figure 24: Electric field magnitude for a single sharp-tip needle.

Chapter 5: Conclusions and Future Work

A series of simulations were performed to determine if an array of laser-fabricated micro-emitters could be used as electric field enhancers in an electrospray thruster. For the geometrical configuration modelled, numerical results indicate that emitters will enhance the applied electric field by a factor of 48 and generate fields strong enough to achieve droplet emission in an electrospray thruster. Optimal emitter spacing, corresponding to maximum possible thrust density attained at the lowest loss of field enhancement, was found to be approximately 20 μm.

Results from simulating a single emitter with a sharp tip, to more closely match actual needle geometry, produced an electric field magnitude of 1.5846×10^9 V/m, indicating PIR emission will be possible. This value is within approximately five percent of the assumed field value of 1.5×10^9 V/m used to calculate the applied voltage, validating this assumption. Given that the increase in electric field magnitude is only due to a change in emitter geometry and not array geometry, and array of sharp tip emitters would be expected to follow the same trends seen in spherical tip simulations. Thus, the optimal emitter spacing should remain at 20 μm. Resolution of mesh discontinuities at points near the tip, and simulations of these arrays are needed to confirm this.

A required voltage of 100 V to 200 V was not obtained, though the 553.33 V voltage found remains approximately half that of what other electrospray thrusters used. Comparison with established electrospray data proved difficult due to lack of available data regarding electric field strengths. It is unknown if these thrusters are using an optimized emitter spacing, as explanations of their spacing choices have not been

found. It is likely that the larger spacings are used due to physical limitations such as wettability of the emitters.

Based on the established results, the next steps in this feasibility study will be to further refine simulation results, as well as explore effects of other design variables, including extractor grid spacing, which was kept constant during these simulations, emitter height and material, and extractor grid geometry. Each of these factors has an impact on thruster performance, and their effects will need to be researched in order to optimize thruster design. Propellant is another factor to explore. Although EMI-BF_4 is currently the preferred propellant, finding an ionic liquid with high electrical conductivity, low surface tension, and that does not contain Fluorine or other toxic reactants would allow for lower voltages while eliminating the risk of generating harmful substances.

References

1. Chiarot, P.R., P. Sullivan, and R. Ben Mrad, *An Overview of Electrospray Applications in MEMS and Microfluidic Systems.* Journal of Microelectromechanical Systems, 2011. **20**(6): p. 1241-1249.
2. Mier-Hicks, F. and P.C. Lozano, *Electrospray Thrusters as Precise Attitude Control Actuators for Small Satellites.* Journal of Guidance, Control, and Dynamics, 2017. **40**(3): p. 642-649.
3. Velasquez-Garcia, L.F., *A Microfabricated Colloid Thruster Array*, in *Aeronautics and Astronautics*. 2001, Massachusetts Institute of Technology. p. 246.
4. Toorian, A., Blundell, E., Puig-Suari, J., and R. Twiggs, *CubeSats as Responsive Satellites*, in *Space 2005*. 2005: Long Beach, CA. p. 14.
5. Chin, A., Coelho, R., Nugent, R., Munakata, R., and J. Puig-Suari, *CubeSat: The Pico-Satellite Standard for Research and Education*, in *AIAA SPACE 2008 Conference & Exposition*. 2008.
6. Velasquez-Garcia, L.F., A.I. Akinwande, and M. Martinez-Sanchez, *A Planar Array of Micro-Fabricated Electrospray Emitters for Thruster Applications.* Journal of Microelectromechanical Systems, 2006. **15**(5): p. 1272-1280.
7. Larriba, C., Castro, S., de la Mora, J.F., and P.C. Lozano, *Monoenergetic source of kilodalton ions from Taylor cones of ionic liquids.* Journal of Applied Physics, 2007. **101**(8).
8. Krejci, D., Mier-Hicks, F., Thomas, R., Haag, T., and P.C. Lozano, *Emission Characteristics of Passively Fed Electrospray Microthrusters with Propellant Reservoirs.* Journal of Spacecraft and Rockets, 2017. **54**(2): p. 447-458.
9. Jahn, R., *Physics of Electric Propulsion*. 1968, McGraw-Hill. p. 142-195.
10. Arestie, S., C. Whitlock, and P.C. Lozano, *Ion Electrospray Propulsion System Feasibility Study for various Satellite Missions and Architectures*, in *49th AIAA/ASME/SAE/ASEE Joint Propulsion Conference*. 2013.
11. Dandavino, S., Ataman, C., Ryan, C.N., Chakraborty, S., Courtney, D., Stark, J. P. W., and H. Shea, *Microfabricated electrospray emitter arrays with integrated extractor and accelerator electrodes for the propulsion of small spacecraft.* Journal of Micromechanics and Microengineering, 2014. **24**(7).
12. Zeleny, J., *The Electrical Discharge from Liquid Points, and a Hydrostatic Method of Measuring the Electric Intensity at Their Surfaces.* Physical Review, 1914. **3**(2): p. 69-91.
13. Taylor, G. *Disintegration of Water Drops in an Electric Field*. in *Royal Society of London Proceedings Series A*. 1964.
14. Martinez-Sanchez, M., *Lecture 23-25: Colloidal Engines*, in *16.522 Space Propulsion*. 2004, Massachusetts Institute of Technology.
15. de la Mora, J.F. and I.G. Loscertales, *The Current Emitted by Highly Conductiing Taylor Cones.* Journal of Fluid Mechanics, 1994. **260**: p. 155-184.
16. Gamero-Castano, M. and V. Hruby, *Electrospray as a source of nanoparticles for efficient colloid thrusters.* Journal of Propulsion and Power, 2001. **17**(5): p. 977-987.
17. Martinez-Sanchez, M. and P. Lozano, *Session 20: Electrospray Propulsion*, in *Space Propulsion 16.522*. 2015, Massachusetts Institute of Technology.
18. Mair, G.L.R., *Emission from Liquid Metal Ion Sources.pdf.* Nuclear Instruments and Methods, 1980. **172**: p. 567-578.

19. Lozano, P. and M. Martinez-Sanchez, *Ionic liquid ion sources: characterization of externally wetted emitters.* J Colloid Interface Sci, 2005. **282**(2): p. 415-21.
20. Velasquez-Garcia, L.F., *The Design Fabrication and Testing of Micro Fabricated Colloid Thruster Arrays*, in *Aeronautics and Astronautics*. 2004, Massachusetts Institute of Technology. p. 276.
21. Martinez-Sanchez, M. and P. Lozano, *Session 24: Ion Emission and the Pure Ionic Regime*, in *Space Propulsion 16.522*. 2015, Massachusetts Institute of Technology.
22. Lozano, P. and M. Martinez-Sanchez, *Ionic liquid ion sources: suppression of electrochemical reactions using voltage alternation.* J Colloid Interface Sci, 2004. **280**(1): p. 149-54.
23. Gamero-Castaño, M. and J. Fernández de la Mora, *Direct measurement of ion evaporation kinetics from electrified liquid surfaces.* The Journal of Chemical Physics, 2000. **113**(2): p. 815-832.
24. Wohlfarth, C., *Surface tension of tributyl phosphate*, in *Surface Tension of Pure Liquids and Binary Liquid Mixtures: Supplement to Volume IV/24*, M.D. Lechner, Editor. 2016, Springer Berlin Heidelberg: Berlin, Heidelberg. p. 14-14.
25. Legge, R. and P. Lozano, *Performance of Heavy Ionic Liquids with Porous Metal Electrospray Emitters*, in *44th AIAA/ASME/SAE/ASEE Joint Propulsion Conference & Exhibit*. 2008.
26. Martino, W., de la Mora, J.F., Yoshida, Y., Saito, G., and J. Wilkes, *Surface tension measurements of highly conducting ionic liquids.* Green Chemistry, 2006. **8**(4).
27. Newth, G.S., *Elementary Inorganic Chemistry*. 1899, New York, NY: Longmans, Green, and Co. 288.
28. Iribarne, J.V., *On the evaporation of small ions from charged droplets.* The Journal of Chemical Physics, 1976. **64**(6).
29. Harris, J.R., K.L. Jensen, and D.A. Shiffler, *Dependence of optimal spacing on applied field in ungated field emitter arrays.* AIP Advances, 2015. **5**(8).
30. Krpoun, R., Raber, M., Shea, H., Smith, K.L., and J.P.W. Stark, *Design and Fabrication of an Integrated MEMS-based Colloid Micropropulsion System*, in *30th International Electric Propulsion Conference*. 2007: Florence, Italy.
31. Alexander, M.S., Stark, J., Smith, K.L., Stevens, B., and B. Kent, *Electrospray Performance of Microfabricated Colloid Thruster Arrays.* Journal of Propulsion and Power, 2006. **22**(3): p. 620-627.
32. Courtney, D., *Ionic Liquid Ion Source Emitter Arrays Fabricated on Bulk Porous Substrates*, in *Aeronautics and Astronautics*. 2011, Massachusetts Institute of Technology. p. 334.
33. Krpoun, R. and H.R. Shea, *Integrated out-of-plane nanoelectrospray thruster arrays for spacecraft propulsion.* Journal of Micromechanics and Microengineering, 2009. **19**(4).
34. Velasquez-Garcia, L.F., A.I. Akinwande, and M. Martinez-Sanchez, *A Micro-Fabricated Linear Array of Electrospray Emitters for Thruster Applications.* Journal of Microelectromechanical Systems, 2006. **15**(5): p. 1260-1271.

35. Courtney, D.G., S. Dandavino, and H. Shea, *Comparing Direct and Indirect Thrust Measurements from Passively Fed Ionic Electrospray Thrusters.* Journal of Propulsion and Power, 2016. **32**(2): p. 392-407.
36. Courtney, D.G., H.Q. Li, and P. Lozano, *Emission measurements from planar arrays of porous ionic liquid ion sources.* Journal of Physics D: Applied Physics, 2012. **45**(48).
37. Krejci, D., Mier-Hicks, F., Fucetola, C., Lozano, P., Schouten, A., and F. Martel, *Design and Characterization of a Scalable ion Electrospray Propulsion System*, in *Joint Conference of 30th International Symposium on Space Technology and Science, 34th International Electric Propulsion Conference and 6th Nano-Satellite Symposium*. 2015: Hyogo-Kobe, Japan.

Appendix

Appendix A: Derivations

A.1: Electric Field of a Surface Instability

As stated in Section 2.2.2, any deformations in a liquid surface will cause any applied field to concentrate in the protruding areas. The resulting traction is balanced by surface charge density, represented by Equation (17) and is repeated here for convenience:

$$\frac{1}{2}\sigma_s E = \frac{1}{2}\varepsilon_0 E^2 \tag{42}$$

Once the electric field becomes strong enough for traction to overcome surface tension, the liquid becomes unstable. This instability will cause a deformation to occur, which will then grow into a shape dependent on the field and container shape and size. Assuming the initial disturbance is small and sinusoidal, a superposition of the applied field and a small perturbation can approximate the outside potential. Using the harmonic function $Re(e^{i\alpha z})$, where $z=x+iy$, the potential approximation is [17]:

$$\phi \approx -E_\infty y + \phi_1 e^{-\alpha y}\cos(\alpha x) \tag{43}$$

At the surface, the potential must meet the condition $\phi = 0$. For $\alpha x << 1$, this condition is met when:

$$0 \approx -E_\infty y + \phi_1 \cos(\alpha x) \tag{44}$$

Rearranging:

$$y \approx \frac{\phi_1 \cos(\alpha x)}{E_\infty} \tag{45}$$

Surface curvature is given by:

$$\frac{1}{R_c} \approx \left|\frac{d^2 y}{dx^2}\right| = \frac{\phi_1 \alpha^2 \cos(\alpha x)}{E_\infty} \tag{46}$$

Equation (46) reaches maximum at $cos(\alpha x) = 1$:

$$R_c = \frac{E_\infty}{\phi_1 \alpha^2} \tag{47}$$

The curvature results in surface tension restoring forces [17] equal to γ/R_c that are normal to the surface. From Equation (43), the normal field is:

$$E_y = -\frac{\partial \phi}{\partial y} = E_\infty + \alpha \phi_1 e^{-\alpha y} \cos(\alpha x) \tag{48}$$

At $cos(\alpha x) = 1$, this reduces to $E_y = E_\infty + \alpha\phi_1$, resulting in an electric traction perturbation of:

$$\delta\left(\frac{1}{2}\varepsilon_0 E_y^2\right) = \varepsilon_0 E_\infty \alpha \phi_1 \tag{49}$$

In order for an instability to occur, this must exceed restoring surface tension effects. Thus:

$$\varepsilon_0 E_\infty \alpha \phi_1 > \gamma \frac{\phi_1 \alpha^2}{E_\infty} \tag{50}$$

Solving for the electric field yields:

$$E_\infty > \sqrt{\frac{\gamma \alpha}{\varepsilon_0}} \tag{51}$$

Equation (51) is thus dependent on surface tension and the quantity α. This quantity is defined as $2\pi/\lambda$, with λ defining the wavelength of the disturbing ripple[17]. This wavelength reaches a maximum when it equals the diameter of the protruding tip, thus $\alpha=\pi/D$. Substituting into Equation (51) results in the instability condition given by Equation (18):

$$E_\infty > \sqrt{\frac{\pi \gamma}{\varepsilon_0 D}} \tag{52}$$

A.2: Starting Voltage at Tip of a Needle

The prolate spheroid shape mentioned in Section 2.2.3 can be plotted using "Prolate Spheroid Coordinates" (Figure 25). Here, $\eta = \frac{r_1 - r_2}{a}$ and $\zeta = \frac{r_1 + r_2}{a}$, with ϕ in this instance being an angle about line FF'. Transformation to Cartesian coordinates is achieved through:

$$r_1 = \sqrt{x^2 + y^2 + \left(z + \frac{a}{2}\right)^2}, \quad r_2 = \sqrt{x^2 + y^2 + \left(z - \frac{a}{2}\right)^2} \tag{53}$$

Surface $\eta = 0$ forms symmetry plane S, and near the needle tip η can define the liquid surface as η_0.

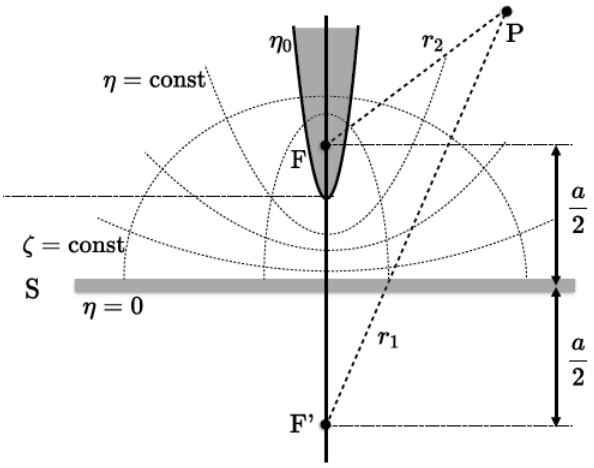

Figure 25: Prolate spheroid coordinate system. [17]

Solving for ϕ depends only on η if it assumed a constant value, V, on $\eta - \eta_0$ and zero at plane S. Laplace's Equation in terms of constant η becomes:

$$\frac{\partial}{\partial \eta}\left[(1 - \eta^2)\frac{\partial \phi}{\partial \eta}\right] = 0 \tag{54}$$

Integrating with the given boundary conditions results in:

$$\phi = V\frac{tanh^{-1}(\eta)}{tanh^{-1}(\eta_0)} \tag{55}$$

If R is defined as a cylindrical radius with $R^2 = x^2 + y^2$, the (z, R) relation for a hyperboloid of constant η is given by:

$$a\eta = \sqrt{R^2 + \left(z + \frac{a}{2}\right)^2} - \sqrt{R^2 + \left(z - \frac{a}{2}\right)^2} \tag{56}$$

For $z > 0$:

$$z = \eta\sqrt{\frac{a^2}{4} + \frac{R^2}{1-\eta^2}} \tag{57}$$

The surface's radius of curvature, R_c, is given by:

$$\frac{1}{R_c} = \frac{z_{RR}}{(1 + z_R^2)^{3/2}} \tag{58}$$

This yields the equation:

$$R_c = a\frac{1-\eta^2}{2\eta}\left[1 + 4\frac{R^2/a^2}{(1-\eta^2)^2}\right] \tag{59}$$

Distance, d, defines the tip-to-plane distance as $d = z(R = 0,\ \eta = \eta_0) = \frac{a}{2}\eta_0$. With R_c and d specified, solving for a and η_0 is possible:

$$a = 2d\sqrt{1 + \frac{R_c}{d}},\quad \eta_0 = \left(1 + \frac{R_c}{d}\right)^{-1/2} \tag{60}$$

At the tip, the Electric Field is found by taking the partial derivative of ϕ with respect to z. In terms of η, this is given as $E_z = -\frac{\partial\phi}{\partial\eta}\frac{\partial\eta}{\partial z}\Big|_{tip}$. With $R = 0$ and $\eta = \eta_0$, this gives $\frac{\partial\eta}{\partial z}\Big|_{tip} = \frac{2}{a}$.

Utilizing equation (A55), the electric field at the tip becomes:

$$E_{tip} = -\frac{2\,V/a}{(1-\eta_0^2)\,tanh^{-1}(\eta_0)} \tag{61}$$

When the characteristic radius and tip-to-plane spacing are chosen such that $R_c << d$, the equation can be expressed as:

$$E_{tip} = -\frac{2V/R_c}{ln(4d/R_c)} \tag{62}$$

This field must be sufficiently strong enough to overcome surface tension forces in order for flow to start. Note that flow will start even in the absence of an applied pressure.

$$\frac{1}{2}\varepsilon_0 E_{tip}^2 > \frac{2\gamma}{R_c} \tag{63}$$

The right-hand side of equation (63) has "2γ" due to an axisymmetric tip having two equal curvatures. Solving (63) for E_{tip} and substituting into equation (62) gives the starting voltage:

$$V_{start} = \sqrt{\frac{\gamma R_c}{\varepsilon_0}}\, ln\left(\frac{4d}{R_c}\right) \tag{64}$$

Vita

Andrew J. Broadbent was born in Oakland, CA, to Andrew P. and Robin A. Broadbent. He was raised in West Chester, PA, where he attended Henderson Senior High School and then Bayard Rustin High School. In 2008, Andrew earned his Eagle Scout Award with BSA Westtown Troop 66. An air and spacecraft fan from an early age, Andrew went to Boston University to study Mechanical Engineering with an Aerospace concentration. After taking a semester off at the beginning of 2011 to sort out some knee problems, he decided to transfer to Lipscomb University, where he graduated with a degree in Mechanical Engineering in 2013. During his time at Lipscomb, his parents moved to Houston, where he moved as well after graduation. After working for two years in the oil field as a Design Engineer, Andrew accepted a graduate research assistantship at the University of Tennessee Space Engineering to pursue a Master's Degree in Aerospace Engineering. At UTSI, Andrew provided research support to the group of Dr. Trevor M. Moeller, as well as assisted in establishing the university's solar observatory. After two and half years, he graduated with his Master of Science in Aerospace Engineering in August 2018.

Permanent email: andrew.broadbent01@gmail.com